The Astrophysical Journal, 809:135 (20pp), 2015 August 20 doi:10.1088/0004-637X/809/2/135

A COORDINATED X-RAY AND OPTICAL CAMPAIGN OF THE NEAREST MASSIVE ECLIPSING BINARY, δ ORIONIS Aa. IV. A MULTIWAVELENGTH, NON-LTE SPECTROSCOPIC ANALYSIS

T. Shenar[1], L. Oskinova[1], W.-R. Hamann[1], M. F. Corcoran[2,3], A. F. J. Moffat[4], H. Pablo[4], N. D. Richardson[4], W. L. Waldron[5], D. P. Huenemoerder[6], J. Maíz Apellániz[7], J. S. Nichols[8], H. Todt[1], Y. Nazé[9,13], J. L. Hoffman[10], A. M. T. Pollock[11], and I. Negueruela[12]

[1] Institut für Physik und Astronomie, Universität Potsdam, Karl-Liebknecht-Str. 24/25, D-14476 Potsdam, Germany
[2] CRESST and X-ray Astrophysics Laboratory, NASA/Goddard Space Flight Center, Greenbelt, MD 20771, USA
[3] Universities Space Research Association, 7178 Columbia Gateway Drive, Columbia, MD 21044, USA
[4] Département de physique and Centre de Recherche en Astrophysique du Québec (CRAQ), Université de Montréal, C.P. 6128, Succ. Centre-Ville, Montréal, Québec, H3C 3J7, Canada
[5] Eureka Scientific, Inc., 2452 Delmer Street, Oakland, CA 94602, USA
[6] Kalvi Institute for Astrophysics and Space Research, MIT, Cambridge, MA, USA
[7] Centro de Astrobiología, INTA-CSIC, Campus ESAC, P.O. Box 78, E-28 691 Villanueva de la Cañada, Madrid, Spain
[8] Harvard-Smithsonian Center for Astrophysics, 60 Garden Street, MS 34, Cambridge, MA 02138, USA
[9] Groupe d'Astrophysique des Hautes Energies, Institut d'Astrophysique et de Géophysique, Université de Liége, 17, Allée du 6 Août, B5c, B-4000 Sart Tilman, Belgium
[10] Department of Physics and Astronomy, University of Denver, 2112 E. Wesley Avenue, Denver, CO 80208, USA
[11] European Space Agency, *XMM-Newton* Science Operations Centre, European Space Astronomy Centre, Apartado 78, E-28691 Villanueva de la Cañada, Spain
[12] Departamento de Física, Ingeniería de Sistemas y Teoría de la Señal, Escuela Politécnica Superior, Universidad de Alicante, P.O. Box 99, E-03 080 Alicante, Spain
Received 2014 December 29; accepted 2015 February 19; published 2015 August 18

ABSTRACT

Eclipsing systems of massive stars allow one to explore the properties of their components in great detail. We perform a multi-wavelength, non-LTE analysis of the three components of the massive multiple system δ Ori A, focusing on the fundamental stellar properties, stellar winds, and X-ray characteristics of the system. The primary's distance-independent parameters turn out to be characteristic for its spectral type (O9.5 II), but usage of the *Hipparcos* parallax yields surprisingly low values for the mass, radius, and luminosity. Consistent values follow only if δ Ori lies at about twice the *Hipparcos* distance, in the vicinity of the σ-Orionis cluster. The primary and tertiary dominate the spectrum and leave the secondary only marginally detectable. We estimate the V-band magnitude difference between primary and secondary to be $\Delta V \approx 2\overset{\mathrm{m}}{.}8$. The inferred parameters suggest that the secondary is an early B-type dwarf (≈B1 V), while the tertiary is an early B-type subgiant (≈B0 IV). We find evidence for rapid turbulent velocities ($\sim$200 km s^{-1}) and wind inhomogeneities, partially optically thick, in the primary's wind. The bulk of the X-ray emission likely emerges from the primary's stellar wind ($\log L_{\mathrm{X}}/L_{\mathrm{Bol}} \approx -6.85$), initiating close to the stellar surface at $R_0 \sim 1.1\,R_*$. Accounting for clumping, the mass-loss rate of the primary is found to be $\log \dot{M} \approx -6.4\,(M_\odot\ \mathrm{yr}^{-1})$, which agrees with hydrodynamic predictions, and provides a consistent picture along the X-ray, UV, optical, and radio spectral domains.

Key words: binaries: close – binaries: eclipsing – stars: early-type – stars: individual ([HD 36486]δOri A) – X-rays: stars

1. INTRODUCTION

Massive stars ($M \gtrsim 10M_\odot$) bear a tremendous influence on their host galaxies, owing to their strong ionizing radiation and powerful stellar winds (e.g., Kudritzki & Puls 2000; Hamann et al. 2006). However, our understanding of massive stars and their evolution still leaves much to be desired. (1) Values of mass-loss rates derived in different studies may disagree with each other by up to an order of magnitude (e.g., Puls et al. 1996; Fullerton et al. 2006; Waldron & Cassinelli 2010; Bouret et al. 2012) and often do not agree with theoretically predicted mass-loss rates (e.g., Vink et al. 2000). (2) The extent of wind inhomogeneities, which greatly influence mass-loss rates inferred by means of spectral analyses, are still largely debated (Shaviv 2000; Owocki et al. 2004; Oskinova et al. 2007; Sundqvist et al. 2011; Šurlan et al. 2013). (3) The production mechanisms of X-ray radiation in massive stars have been a central subject of study in recent decades (Feldmeier et al. 1997; Pollock 2007) and are still far from being understood. (4) The effect of magnetic fields and stellar rotation on massive stars (e.g., Friend & MacGregor 1984; Maheswaran & Cassinelli 2009; Oskinova et al. 2011; de Mink et al. 2013; Petit et al. 2014; Shenar et al. 2014), e.g., through magnetic braking (Weber & Davis 1967) or chemical mixing (Maeder 1987), are still being investigated. (5) Lastly, stellar multiplicity seems to play a fundamental role in the context of massive stars, significantly affecting their evolution (e.g., Eldridge et al. 2013).

Several studies in the past years (e.g., Mason et al. 2009; Maíz Apellániz 2010; Chini et al. 2012; Sana et al. 2013; Aldoretta et al. 2014; Sota et al. 2014) give direct evidence that at least half of the massive stars are found in multiple systems. Massive stars in close binary systems generally evolve differently from single stars. Such systems may experience significant tidal forces (Zahn 1975; Palate et al. 2013), mass-transfer (Pols et al. 1991), additional supernova kicks (Hurley et al. 2002), and mutual irradiation effects (Howarth 1997). Given the large binary fraction, an understanding of these processes is critical to properly model the evolution of massive stars. Fortunately, binary systems have two main advantages

[13] FNRS Research Associate.

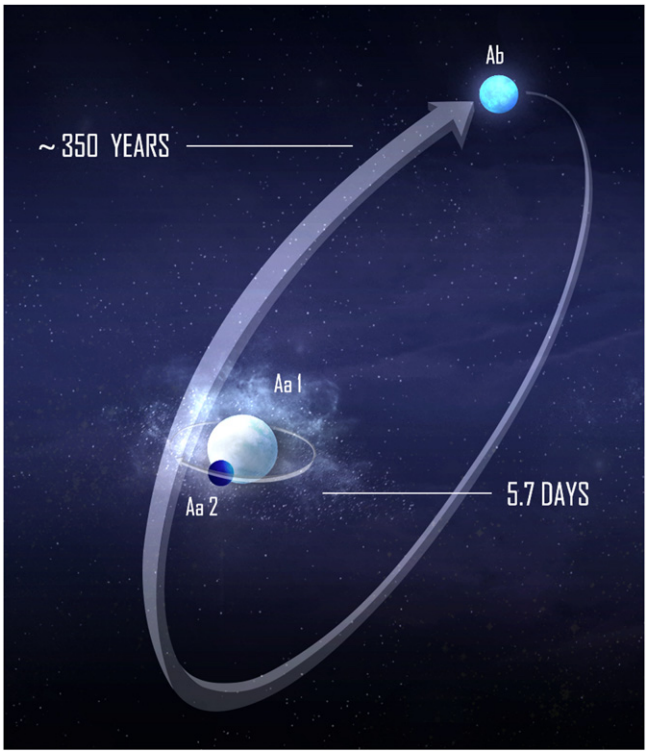

Figure 1. Artist's impression of the triple system δ Ori A, as viewed from Earth. The primary (Aa1) and Secondary (Aa2) form the tight eclipsing binary of a period of 5.7 days. The primary shows evidence for a significant wind in all spectral domains. A third star (Ab) at an angular separation of $\approx 0\farcs3$ ($\sim$100 AU at a distance of $d = 380$ pc to Earth) orbits the system with a period of $\approx$346 years (Tokovinin et al. 2014) and contributes roughly 25% to the total visual flux. The sizes of all three components are drawn to scale, as inferred in this collaborative study. Their colors reflect their relative temperatures. Note that the tertiary is the second brightest companion in the system. The distance between the binary system Aa and the tertiary Ab is not to scale. Credits to Jessica Mayo.

over single stars. First, they offer us the opportunity to empirically determine stellar masses. Second, eclipsing binary systems provide the unique opportunity to investigate different characteristics of stellar winds by taking advantage of occultation (e.g., Antokhin 2011). It is therefore insightful to analyze eclipsing multiple systems of massive stars in our Galactic neighborhood, using adequate, state-of-the-art modeling tools.

The star δ Ori A (HD 36 486, Mintaka, HIP 25 930, HR 1852) is a massive triple system (see artist's illustration in Figure 1) comprised of the close eclipsing binary Aa (primary Aa1, secondary Aa2) with a 5.732-day period (Harvey et al. 1987; Harvin et al. 2002; Mayer et al. 2010), and the more distant tertiary Ab at an angular separation of $\approx 0\farcs3$ relative to the binary Aa with a period of $\sim$346 years (Heintz 1980; Perryman & ESA 1997; Tokovinin et al. 2014). The tertiary Ab has been photometrically resolved from the binary Aa in different surveys (Horch et al. 2001; Mason et al. 2009; Maíz Apellániz 2010) and is found to contribute $\approx$25% to the system's flux in the visual band. These three components are not to be confused with the more distant and significantly fainter stars δ Ori B and C at separations of 33″ and 53″, respectively; together, these five stars comprise the multiple system δ Ori, also known as Mintaka. With a visual magnitude of $V = 2\fm24$ outside eclipse (Morel & Magnenat 1978), δ Ori A is one of the brightest massive multiple systems in the night sky, making it easily visible to the naked eye (it is the westmost star in Orion's belt). According to the new *Hipparcos* reduction (van Leeuwen 2007), its parallax is 4.71 ± 0.58 mas, corresponding to a distance of $d = 212 \pm 30$ pc.[14] On the other hand, the system resides in the Orion OB1b association, to which the σ-Orionis cluster belongs as well. The distance to the cluster itself is estimated to be $d \sim 380$ pc, almost a factor of two larger than the *Hipparcos* distance (see Caballero & Solano 2008 and references therein).

This paper is a contribution to a series of papers within the framework of the δ Ori collaboration. The other papers include the analysis of high quality *Chandra* observations to explore X-ray properties (Corcoran et al. 2015; Paper I) and variability (Nichols et al. 2015; Paper II) in the system, and a complete photometric and spectrometric variabilty analysis (Pablo et al. 2015; Paper III). In this study, we focus on a non-LTE, multiwavelength spectral analysis of the three components Aa1, Aa2, and Ab, with the goal of obtaining reliable stellar and wind parameters.

δ Ori A has been repeatedly studied previously. The system, which shows clear evidence for a significant stellar wind in the optical, UV, and X-ray domains, has been assigned the spectral type O9.5 II (Walborn 1972), later refined by Sota et al. (2011) to O9.5 II Nwk, which most probably corresponds to the brigtest component: Aa1. With less confidence, the secondary Aa2 has been assigned the spectral type B0.5 III (Harvin et al. 2002). This result is questioned by Mayer et al. (2010), who argue that the secondary is too faint for this spectral type. The latter authors further suggest the spectral type O9 IV for the tertiary and leave the secondary unclassified.

Although the stellar parameters of an eclipsing stellar system can usually be sharply constrained, much controversy is found in the literature in the case of δ Ori A. Koch & Hrivnak (1981) reported $M_1 = 23\,M_\odot$, $R_1 = 17\,R_\odot$ and $M_2 = 9\,M_\odot$, $R_2 = 10\,R_\odot$ for the primary and secondary masses and radii, respectively, as well as a V-band magnitude difference of $\Delta V_{\rm Aa1Aa2} = 1\fm4$. Harvin et al. (2002) later inferred significantly smaller masses for the primary and secondary, $M_1 = 11.2\,M_\odot$, $M_2 = 5.6\,M_\odot$, and a smaller contribution of the secondary in the visual band: $\Delta V_{\rm Aa1Aa2} = 2\fm5$. These results were challenged by Mayer et al. (2010), who suggested that a confusion between the secondary Aa2 and tertiary Ab led to the low masses obtained by Harvin et al. (2002). Mayer et al. (2010) inferred $R_1 = 15.6\,R_\odot$ and $R_2 = 4.8\,R_\odot$. They did not detect any contribution from the secondary Aa2 and concluded that $\Delta V_{\rm Aa1Aa2} \gtrsim 3\fm5$. Assuming $M_1 = 25\,M_\odot$, they inferred $M_2 = 9.9\,M_\odot$. In Paper III, the secondary's radial velocity (RV) curve could not be constructed, and, for an adopted primary mass of $M_1 \approx 24\,M_\odot$, it was concluded that $M_2 = 8.5\,M_\odot$ $R_1 = 15.1\,R_\odot$, $R_2 = 5.0\,R_\odot$.

Similarly, reported values of the mass-loss rate of the primary are quite diverse: Lamers & Leitherer (1993) report $\log \dot{M}_1 = -5.97\,(M_\odot\ {\rm yr}^{-1})$ based on radio observation and $\log \dot{M}_1 = -5.92\,(M_\odot\ {\rm yr}^{-1})$ based on Hα analysis. Lamers et al. (1999) later similarly obtain $\log \dot{M}_1 = -5.7\,(M_\odot\ {\rm yr}^{-1})$ based on P Cygni profile analysis using the Sobolev plus exact integration method. Neglecting the effects of wind inhomogeneities and porosity (Oskinova et al. 2007; Šurlan

[14] This value is not corrected for the Lutz–Kelker effect (Lutz & Kelker 1973). Maíz Apellániz et al. (2008) account for this effect and revise the distance to $d = 221$ pc. However, the difference is negligible within measurement uncertainties.

et al. 2013) on the observed X-ray spectrum, and adopting a generic O-type model, Cohen et al. (2014) derived a value of $\dot{M}_1 = -7.2\,(M_\odot\ \mathrm{yr}^{-1})$ from X-ray line profile fitting, more than an order of magnitude less than the previously inferred value. Indeed, no consensus on the mass-loss rate of the primary has been reached so far.

δ Ori A has an observed X-ray luminosity of $L_X \approx 1.4 \cdot 10^{32}\,\mathrm{erg\,s^{-1}}$for $d = 380$ pc (Paper I). δ Ori A's X-ray properties were previously explored by Miller et al. (2002), Leutenegger et al. (2006), and Raassen & Pollock (2013). These studies generally identify the X-ray formation process to be intrinsic to the primary's wind, a result that is further supported within our collaboration. An extensive review of past X-ray observations and analyses are given by Paper I and II.

In this study, we perform a consistent non-LTE photosphere and wind analysis of the three components of the triple system δ Ori A in the optical, UV, and X-ray domains, at several orbital phases. We analyze the optical and UV spectra using the non-LTE Potsdam Wolf–Rayet (PoWR) code, which is applicable to any hot star. We further illustrate the importance of optically thin and optically thick clumps in the wind. We use the non-LTE models to simulate the effect of X-rays in the wind of the primary and derive onset radii of X-ray formation regions using ratios of forbidden and intercombination lines in the *Chandra* spectra. Finally, using the non-LTE model of the primary, we calculate synthetic X-ray line profiles and compare them to observed ones. Our results are further compared to studies of the radio emission from the system. This study thus encompasses the whole range from the X-ray domain to the radio domain.

The structure of the paper is as follows. In Section 2, we describe the observational data used. Our modeling methods and assumptions are discussed in Section 3. In Section 4, we present and discuss our results. Section 5 focuses on the effect of wind inhomogeneities on the optical, UV, and X-ray spectral domains, while, in Section 6, we study the X-ray radiation of the star. Lastly, in Section 7, we summarize our results.

2. OBSERVATIONAL DATA

All spectra used in this analysis contain the contribution of the primary Aa1, secondary Aa2, and tertiary Ab. In the following, all phases given are photometric phases relative to primary minimum (occurring when the secondary occults the primary), calculated with $E_0 = \mathrm{HJD}\ 2456277.79$ d and $P = 5.732436$ d (Paper III and references therein).

Two of our optical spectra are of high resolution and high signal-to-noise ratio (S/N), obtained with the NARVAL spectropolarimeter on 2008 October 23 and 24. These spectra were reduced with standard techniques and downloaded from the PolarBase[15] (Petit et al. 2014). The observations were carried out with the Telescope Bernard Lyot. The spectra have an S/N of 500–800, and correspond to phases $\phi = 0.84$ and $\phi = 0.02$.

Three additional optical spectra at phases $\phi = 0.19$, 0.38, and 0.54 were obtained on the nights of 2012 December 28, 29, and 30 (contemporaneous with our *Chandra* and *MOST* observations) using the CAFÉ spectrograph at the 2.2 m Calar Alto telescope as part of the CAFÉ-BEANS project, a survey that is obtaining high-resolution ($R \sim 65{,}000$) multi-epoch optical spectroscopy of all bright O stars in the northern hemisphere to complement OWN, the equivalent southern hemisphere survey (Barbá et al. 2010; Sota et al. 2014). On each date, 10 consecutive 30 s exposures were obtained and combined to yield spectra with S/N varying from ~200 in the blue part (~4500 Å) to ~500 in the red part (~6000 Å). The data were processed using a pipeline developed specifically for the project. The velocity stability was checked using ISM lines. More details regarding the reduction pipeline are given by Negueruela et al. (2014).

For the spectral range 1200–2000 Å, we make use of archival *IUE* spectra at different orbital phases (see the observation log given by Harvin et al. 2002). The spectra have an S/N of $\sim 10\ \mathrm{pixel}^{-1}$, and are averaged in bins of 0.1 Å. The *IUE* spectra are flux-calibrated and are rectified using the model continuum.

In the spectral range 1000–1200 Å, we make use of the *Copernicus* observation available in the *Copernicus* archive under the ID c025-001.u2. This observation consists of 48 co-added scans obtained between 1972 November 21 and 24.

For the spectral energy distribution (SED), we make use of *U*, *B*, *V*, *R*, *I*, *J*, *H*, *K* (Morel & Magnenat 1978), *WISE* (Cutri et al. 2012), and *IRAS* (Moshir et al. 1990) photometry. We further use a low-resolution, flux calibrated optical spectrum kindly supplied to us by S. Fabrika & A. Valeev (2015, private communication). The spectrum was obtained with the Russian BTA telescope using the SCORPIO focal reducer, on 2013 December 31 in the range of 3800–7200 Å with a spectral resolution of 6.3 Å, and corresponds to phase $\phi = 0.42$. A Hartmann mask was used to avoid saturation.

The *Chandra* X-ray spectra used in Section 6 were taken with the HEG and MEG detectors for a total exposure time of 487.7 ks. The data are thoroughly described in Paper I and II.

3. NON-LTE PHOTOSPHERE AND WIND MODELING

3.1. The PoWR Code

PoWR is a non-LTE model atmosphere code especially suitable for hot stars with expanding atmospheres.[16] The code consists of two main parts. In the first part, referred to as the non-LTE iteration, the co-moving frame radiative transfer in spherical symmetry and the statistical balance equations are solved in an iterative scheme under the constraint of energy conservation, yielding the occupation numbers in the photosphere and wind. The second part, referred to as the formal integration, delivers a synthetic spectrum in the observer's frame. The pre-specified wind velocity field takes the form of a β-law (Castor et al. 1975) in the supersonic region. In the subsonic region, the velocity field is defined so that a hydrostatic density stratification is approached. Line blanketing by the iron lines is treated in the superlevel approach (Gräfener et al. 2002), as originally introduced by Anderson (1989). A closer description of the assumptions and methods used in the code is given by Gräfener et al. (2002) and Hamann & Gräfener (2004).

In the non-LTE iteration, line profiles are Gaussians with a constant Doppler width v_{Dop}. In the formal integration, the Doppler velocity is composed of depth-dependent thermal motion and microturbulence. The microturbulence $\xi(r)$ is interpolated between the photospheric microturbulence

[15] http://polarbase.irap.omp.eu

[16] PoWR models of Wolf–Rayet stars can be downloaded at http://www.astro.physik.uni-potsdam.de/PoWR.html.

$\xi(r_{\rm ph}) = \xi_{\rm ph}$ and the wind microturbulence $\xi(r_{\rm w}) = \xi_{\rm w}$, with the radii $r_{\rm ph}$ and $r_{\rm w}$ pre-specified. Thermal and pressure broadening are accounted for in the formal integration. Turbulence pressure is also accounted for in the non-LTE iteration. Optically thin wind inhomogeneities are accounted for in the non-LTE iteration using the so-called "microclumping" approach (Hamann et al. 1995). The density contrast between a clumped and a smooth wind with an identical mass-loss rate is described by the depth-dependent clumping factor $D(r)$ (Hamann & Koesterke 1998), where the clumps are assumed to be optically thin. Optically thick clumps, or "macroclumps," are accounted for in the formal integration as described by Oskinova et al. (2007), where the clump separation parameter $L_{\rm mac}$ is to be specified (see Section 5).

Four fundamental input parameters define a model atmosphere of an OB type star: T_*, L, g_*, $\dot{M}$. T_* is the effective temperature of a star with luminosity L and radius R_*, as defined by the Stefan–Boltzmann relation $L = 4\pi\sigma R_*^2 T_*^4$. g_* is related to the radius R_* and mass M_* via $g_* = g(R_*) = G\,M_* R_*^{-2}$. $\dot{M}$ is the mass-loss rate of the star. The stellar radius R_* is defined at the continuum Rosseland optical depth $\tau_{\rm Ross} = 20$, which is the inner boundary of our model, and which was tested to be sufficiently large. The outer boundary of the model is set to $100\,R_*$. Note that the stellar radius is generally not identical to the photospheric radius $R_{2/3}$ defined at $\tau_{\rm Ross} = 2/3$. However, usually $R_* \cong R_{2/3}$, except in cases of extreme radiation pressures (e.g., supergiants, Wolf–Rayet stars). Nevertheless, one must bear in mind that the effective temperature referring to the photospheric radius, which we denote with $T_{2/3}$ to avoid ambiguity, may slightly differ from T_*. Similarly, $g_{2/3} = g(R_{2/3})$ is the gravity at $\tau_{\rm Ross} = 2/3$. Like most studies, we specify photospheric values when compiling our results in Table 1, but the cautious reader should be aware of this difference when comparing with other studies.

Due to the strong radiative pressures in massive stars, one cannot measure the gravity g_* directly from their spectra, but rather the effective gravity $g_{\rm eff}$. g_* is obtained from $g_{\rm eff}$ via $g_{\rm eff} := g_*\left(1 - \overline{\Gamma}_{\rm rad}\right)$, where $\overline{\Gamma}_{\rm rad}$ is a weighted average of the ratio of total outward radiative force to inward gravitational force over the hydrostatic domain. The outward radiative force is calculated consistently in the non-LTE iteration, and includes the contribution from line, continuum, and Thomson opacities (Sander et al. 2015).

3.2. The Analysis Method

The analysis of stellar spectra with non-LTE model atmosphere codes is an iterative, computationally expensive process that involves a multitude of parameters. Nevertheless, most parameters affect the spectrum uniquely. Generally, the gravity g_* is inferred from the wings of prominent hydrogen lines. The stellar temperature T_* is obtained from the line ratios of ions belonging to the same element. Wind parameters such as $\dot{M}$, v_∞, and $L_{\rm mac}$ are derived from emission lines, mainly in the UV. The luminosity L and the color excess $E(B-V)$ are determined from the observed SED, and from flux-calibrated spectra. The abundances are determined from the overall strengths of lines belonging to the respective elements. Finally, parameters describing the various velocity fields in the photosphere and wind (rotation, turbulence) are constrained from profile shapes and strengths. The radius R_* and spectroscopic mass M_* follow from L, T_*, and g_*.

To analyze a multiple system such as δ Ori A, a model for each component star is required. As opposed to single stars, the luminosities of the components influence their contribution to the overall flux and thus affect the normalized spectrum. The light ratios of the different components therefore become entangled with the fundamental stellar parameters. Fortunately, with fixed temperatures and gravities for the secondary and tertiary components, the observational constraints provide us with the light ratios (see Section 3.3).

Methods to disentangle a composite spectrum into its constituent spectral components by observing the system at different phases have been proposed and implemented during the past few years (Bagnuolo & Gies 1991; Simon & Sturm 1994; Hadrava 1995; González & Levato 2006; Torres et al. 2011). In fact, an attempt to disentangle the spectrum of δ Ori A was pursued by Harvin et al. (2002) and Mayer et al. (2010). However, even after performing the disentanglement, the two sets of authors come to significantly different results. A disentanglement of the He I λ6878 line was performed in Paper III, but, after accounting for the contribution of the tertiary as obtained here, no clear signal from the secondary was detected. Given the very low contribution of the secondary Aa2, and having only poor phase coverage in the optical, we do not pursue a disentanglement of δ Ori A.

As a first step, the secondary and tertiary models are kept fixed. Motivated by the results of Paper III, we initially adopt $T_{2/3} \sim 25$ kK and $\log g_{2/3} \sim 4.15\,({\rm g\,cm^{-2}})$ for the secondary. The tertiary is initially fixed with the parameters suggested by Mayer et al. (2010). With the light ratios at hand, this fixes the luminosities of Aa2 and Ab. Having fixed the secondary and tertiary models, we turn to the second step, which is an accurate analysis of the primary.

To constrain T_*, we use mostly He I and He II lines, such as He I $\lambda\lambda$ 4026, 4144, 4388, 4713, 4922, 5015, 6678 and He II λ4200, 4542, 5412, 6683. The prominent He II λ4686 line is found to be a poor temperature indicator (see Section 4.2). The temperature is further verified from lines of carbon, nitrogen, and silicon. g_* is primarily derived from the wings of prominent Balmer and He II lines. Here we encounter the difficult problem of identifying the contribution of the tertiary to the hydrogen lines due to the pronounced wings of the Balmer lines. We therefore also made use of diagnostic lines such as C III λ5696, whose behavior heavily depends on the gravity (see Section 4.4).

$\dot{M}$ and $L_{\rm mac}$ follow from a simultaneous fitting of Hα and UV P Cygni lines. The wind parameters are checked for consistency with previous analyses of radio observations and with X-ray observations (see Section 6.3). The terminal velocity v_∞ is determined from UV resonance lines. However, v_∞ can only be determined accurately after the wind microturbulence has been deduced. The determination of the projected rotational velocity $v \sin i$ and of the inner (photospheric) and outer (wind) microturbulent velocities $\xi_{\rm ph}$ and $\xi_{\rm w}$, as well as of the macroturbulent velocity $v_{\rm mac}$, is discussed in detail in Section 4.3.

The abundances are determined from the overall strengths of lines belonging to the respective elements. We include the elements H, He, C, N, O, Mg, Al, Si, P, and S, as well as elements belonging to the iron group (e.g., Fe, Ni, Cr etc.).

Table 1
Inferred Stellar Parameters for the Multiple Stellar System δ Ori A

	Aa1		Aa2		Ab	
$T_{2/3}$ (kK)	29.5 ± 0.5		25.6 ± 3000		28.4 ± 1500	
log $g_{\rm eff}$ (cm s^{-2})	3.0 ± 0.15		3.7		3.2 ± 0.3	
log $g_{2/3}$ (cm s^{-2})	3.37 ± 0.15		3.9		3.5 ± 0.3	
v_∞ (km s^{-1})	2000 ± 100		1200		2000	
D	10		10		10	
$L_{\rm mac}$ ($R_\odot$)	$\gtrsim$0.5		...		...	
$E(B-V)$ (mag)	0.065 ± 0.01		0.065 ± 0.01		0.065 ± 0.01	
A_V (mag)	0.201 ± 0.03		0.201 ± 0.03		0.201 ± 0.03	
$v \sin i$ (km s^{-1})	130 ± 10		150 ± 50		220 ± 20	
$\xi_{\rm ph}$ (km s^{-1})	20 ± 5		10		10 ± 5	
$\xi_{\rm w}$ (km s^{-1})	200 ± 100		10		10	
$v_{\rm mac}$ (km s^{-1})	60 ± 30		0		50 ± 30	
H (mass fraction)	0.70 ± 0.05		0.7		0.7	
He (mass fraction)	0.29 ± 0.05		0.29		0.29	
C (mass fraction)	2.4 ± 1 × 10^{-3}		2.4 × 10^{-3}		2.4 × 10^{-3}	
N (mass fraction)	4.0 ± 2 × 10^{-4}		7.0 × 10^{-4}		7.0 × 10^{-4}	
O (mass fraction)	6.0 ± 2 × 10^{-3}		6.0 × 10^{-3}		6.0 × 10^{-3}	
Mg (mass fraction)	6.4 × 10^{-4}		6.4 × 10^{-4}		6.4 × 10^{-4}	
Al (mass fraction)	5.6 × 10^{-5}		5.6 × 10^{-5}		5.6 × 10^{-5}	
Si (mass fraction)	4 ± 2 × 10^{-4}		6.6 × 10^{-4}		6.6 × 10^{-4}	
P (mass fraction)	5.8 × 10^{-6}		5.8 × 10^{-6}		5.8 × 10^{-6}	
S (mass fraction)	3.0 × 10^{-4}		3.0 × 10^{-4}		3.0 × 10^{-4}	
Fe(mass fraction)	1.3 × 10^{-3}		1.3 × 10^{-3}		1.3 × 10^{-3}	
Adopted distance d (pc)	212	380	212	380	212	380
log L ($L_\odot$)	4.77 ± 0.05	5.28 ± 0.05	3.7 ± 0.2	4.2 ± 0.2	4.3 ± 0.15	4.8 ± 0.15
log $\dot{M}$ ($M_\odot$ yr^{-1})	−6.8 ± 0.15	−6.4 ± 0.15	−8.5	−8.1	$\leqslant$−7.0	$\leqslant$−6.6
$M_{\rm spec}$ ($M_\odot$)	$7.5^{+3}_{-2.5}$	24^{+10}_{-8}	2.6	8.4	7.0^{+7}_{-4}	22.5^{+24}_{-14}
$R_{2/3}$ ($R_\odot$)	9.2 ± 0.5	16.5 ± 1	3.6 ± 1	$6.5^{+2}_{-1.5}$	5.8 ± 1	10.4 ± 2
M_V (mag)	−4.47 ± 0.13	−5.74 ± 0.13	−1.7 ± 0.5	−3.0 ± 0.5	−3.2 ± 0.4	−4.5 ± 0.4

With the remaining stellar parameters fixed, this is a straightforward procedure.

The total bolometric luminosity $L = L_1 + L_2 + L_3$ is obtained by fitting the synthetic flux with the observed SED. The individual component luminosities follow from the light ratios. The color excess E_{B-V} is derived using extinction laws published by Cardelli et al. (1989) with $R_V = 3.1$, and can be very accurately determined from flux-calibrated *IUE* observations. The inferred value for A_V is consistent with those of Maíz Apellániz & Sota (2015, in preparation), who obtain a value of 0.185 ± 0.013 mag using Tycho+Johnson +2MASS photometry and the extinction laws of Maíz Apellániz et al. (2014).

After obtaining a satisfactory model for the primary, we continue to iterate on the secondary and tertiary models by identifying small deviations between the composite synthetic and observed spectra at different orbital phases, as described in Section 4.2. This allows us to adjust the temperatures and gravities of both models, as well as of the projected rotation velocities. After improving the secondary and tertiary models, we return to the primary and adjust the model parameters accordingly. We repeat this process several times until a satisfactory fit is obtained in the UV and optical, taking hundreds of lines into account in this process.

3.3. Initial Assumptions

Given the large number of parameters involved in this analysis, it is advisable to initially fix parameters that are constrained based on observations, previous studies, and theoretical predictions.

We adopt $\beta = 0.8$ for the exponent of the β-law for all components, which is both supported by observations as well as theoretically predicted (e.g., Kudritzki et al. 1989; Puls et al. 1996). Varying this parameter in the range 0.7–1.5 did not significantly affect the resulting synthetic spectrum.

A V-band magnitude difference of $\Delta V_{\rm AaAb} = 1\overset{\rm m}{.}35$ between the binary system Aa (composed of Aa1 and Aa2) and the tertiary Ab was measured by the *Hipparcos* satellite (Perryman & ESA 1997). Horch et al. (2001) report $\Delta V_{\rm AaAb} = 1\overset{\rm m}{.}59$, obtained from speckle photometry. Mason et al. (2009) find $\Delta V_{\rm AaAb} = 1\overset{\rm m}{.}4$ by means of speckle interferometry. Like Mayer et al. (2010), we adopt $\Delta V_{\rm AaAb} = 1\overset{\rm m}{.}4$, corresponding to the flux ratio $R_{\rm AaAb} \coloneqq F_V({\rm Aa})/F_V({\rm Ab}) = 3.63$. As for the binary components Aa1 and Aa2, additional information regarding $\Delta V_{\rm Aa1Aa2}$ can be obtained from the visual light curve of the system δ Ori A. The secondary light curve minimum (primary star in front) has a depth $\Delta V_{\rm II.\ min} \approx 0\overset{\rm m}{.}055$ with an error of about $0\overset{\rm m}{.}005$. Since the secondary eclipse is partial (Paper III), the secondary minimum yields a lower limit to

$R_{\rm Aa2Aa1}$. One obtains after some algebra

$$R_{\rm Aa2Aa1} \geqslant \frac{(R_{\rm II.min} - 1)(R_{\rm AaAb} + 1)}{R_{\rm AaAb} - R_{\rm II.min} + 1}. \quad (1)$$

In our case, $R_{\rm AaAb} \approx 3.63$ and $R_{\rm II.min} \approx 1.05$, and so $F_V({\rm Aa2}) \gtrsim 0.07\, F_V({\rm Aa1})$, which in turn implies $\Delta V_{\rm Aa1Aa2} \lesssim 2\overset{\rm m}{.}9$. It follows that the secondary Aa2 contributes *at least* 6.5% to the visual flux of the binary, and *at least* 5.1% to the total visual flux of the system. We thus initially assume $\Delta V_{\rm Aa2Aa1} = 2\overset{\rm m}{.}8$, and further constrain this value in the spectral analysis (see Section 4.1).

In Section 4.1, we show that usage of the *Hipparcos* distance $d = 212$ pc results in extremely peculiar parameters for the primary given its spectral type, and that a much better agreement is obtained for the alternative distance of the neighboring stellar cluster σ-Orionis, $d \sim 380$ pc (see also the discussion by Simón-Díaz et al. 2015). We therefore refer to both distances in the following and discuss this issue more thoroughly in Section 4.1. We note, however, that our results can be easily scaled with the distance, should it be revised in future studies (see Section 4).

As we illustrate in Section 5, there are several indications for wind inhomogeneities (clumps) in the wind of Aa1. While clumping may already initiate at sub-photospheric layers, e.g., due to sub-photospheric convection (Cantiello et al. 2009), we avoid an attempt to treat clumpiness in the optically thick layers below the photosphere. For reasons that are discussed in detail in Section 5, we adopt a depth-dependent clumping factor $D(r)$ that is fixed to one (no clumping) in the domain $R_* \leqslant r \leqslant 1.1\, R_*$ and reaches a maximum value of $D_{\rm max} = 10$ at $r \geqslant 10\, R_*$.

Due to the faintness of the secondary and tertiary, we can only give upper limits to their mass-loss rates, and set their terminal velocities to be 2.6 times their escape velocity (Lamers & Cassinelli 1999). We further assume $\xi(r) = 10\,{\rm km\,s^{-1}}$ for the secondary, a typical value for OB-type stars of luminosity classes III and lower (see Villamariz & Herrero 2000 and references therein). We choose to adopt an identical density contrast $D(r)$ for all three models. Finally, we do not attempt to constrain the abundances in the secondary and tertiary, but rather adopt solar values (Asplund et al. 2009). This set of assumptions should bear very little effect on the derived fundamental parameters of the three components.

4. RESULTS

The stellar parameters inferred for the three components are given in Table 1. The model of the primary includes the effect of macroclumping and X-rays, which we thoroughly discuss in Sections 5 and 6. The upper part of the table displays parameters that, to first order, do not depend on the adopted distance. The lower part of the table denotes distance-dependent parameters. For the convenience of the reader, we give these parameters for both "candidate" distances, $d = 212$ pc and $d = 380$ pc. Luminosities scale as $L \propto d^2$, mass-loss rates as $\dot{M} \propto d^{3/2}$, radii as $R_* \propto d$, and the mass as $M_{\rm spec} \propto d^2$. The error margins given in Table 1 are discussed in Section 4.4 and are based on the sensitivity of our analysis to these parameters. Values without errors that are not upper bounds indicate adopted values.

The upper panel of Figure 2 displays the synthetic SEDs for the models of the three components of the system. The total synthetic SED (red solid line) comprises the synthetic fluxes of the primary Aa1 (green dashed line), secondary Aa2 (gray dot–dashed line), and tertiary Ab (pink dotted line). Recall that the tertiary is brighter than the secondary. The blue squares denote *U*, *B*, *V*, *R*, *I*, *J*, *H*, *K*, *WISE*, and *IRAS* photometry. We also plot two observed flux-calibrated spectra in the UV and optical (blue lines). The lower panels of Figure 2 show the composite synthetic (red dotted line) and observed (blue line) normalized UV and optical spectra of the system. The optical spectrum and the UV spectrum in the range 1200–2000 Å correspond to phase $\phi \approx 0.54$. The synthetic normalized spectrum consists of three models calculated for Aa1, Aa2, and Ab, shifted according to their RVs. The synthetic spectra are convolved with a Gaussian of FWHM = 0.1 Å to account for instrumental broadening, inferred from fitting of the interstellar Na I $\lambda\lambda$5890, 5896.3 lines. We do not plot the individual spectra of the three components for clarity. Note that the wavy pattern seen in the observed spectrum (e.g., in the domain 5900–6500 Å) is an artifact that originates in the connection of the echelle orders, not related to the stellar system.

It is evident that both the synthetic SED and normalized spectrum agree well with the observed spectrum. A good balance is obtained for all He I lines and He II lines, as well as for the metal lines. The inferred parameters for microturbulence, rotation, and macroturbulence yield consistent line strengths and profiles over the whole spectral domain. The pseudo continuum formed by the iron forest in the range of 1300–1800 Å, as well as most photospheric and wind features, are well reproduced.

The few features that are not reproduced very well are the Balmer lines, and especially Hδ. Hδ has a significantly smaller observed EW (≈1.85 Å) compared to the synthetic spectrum (≈2.35 Å). In fact, the observed EW of Hδ is somewhat smaller than usual for similar spectral types (e.g., Cananzi et al. 1993), and the question arises as to the cause. A significantly smaller gravity for the primary does not agree with the wing shape of the other Balmer and He II lines and hardly affects the EW. Reducing the hydrogen abundance of the primary implies a larger helium abundance, which is not consistent with the helium lines. Larger $\dot{M}$ values lead to very strong emission in Hα, which is not observed. The photospheric microturbulence has only negligible effect on the EW of hydrogen lines. We therefore conclude that the Balmer lines are diluted by the light of one or both of the other components. However, the low EW of Hδ could only be reproduced when assuming very peculiar parameters for the tertiary, e.g., a very weak gravity ($\log g_{2/3} \lesssim 3.2\,({\rm g\,cm^{-2}})$), or very large mass-loss rates ($\log \dot{M} \gtrsim -5.5\,\left(M_\odot\ {\rm yr^{-1}}\right)$). Such parameters are not only hard to justify physically, but also not consistent with the remaining spectral lines. The problem is also seen, albeit to a lesser extent, in the lines Hγ and Hβ. Future observations should shed light on this peculiarity.

4.1. Which Distance is the Correct one?

It is reassuring that those fundamental stellar parameters of the primary that do not depend on the distance match well with its spectral type. Interpolating calibrations by Martins et al. (2005) to an O9.5 II class yields $T_{2/3} = 29.3$ kK and $\log g_{2/3} = 3.35\,({\rm g\,cm^{-2}})$, which agrees with our results within the error margins. The primary's nitrogen and silicon abundances are found to be slightly subsolar. It is interesting

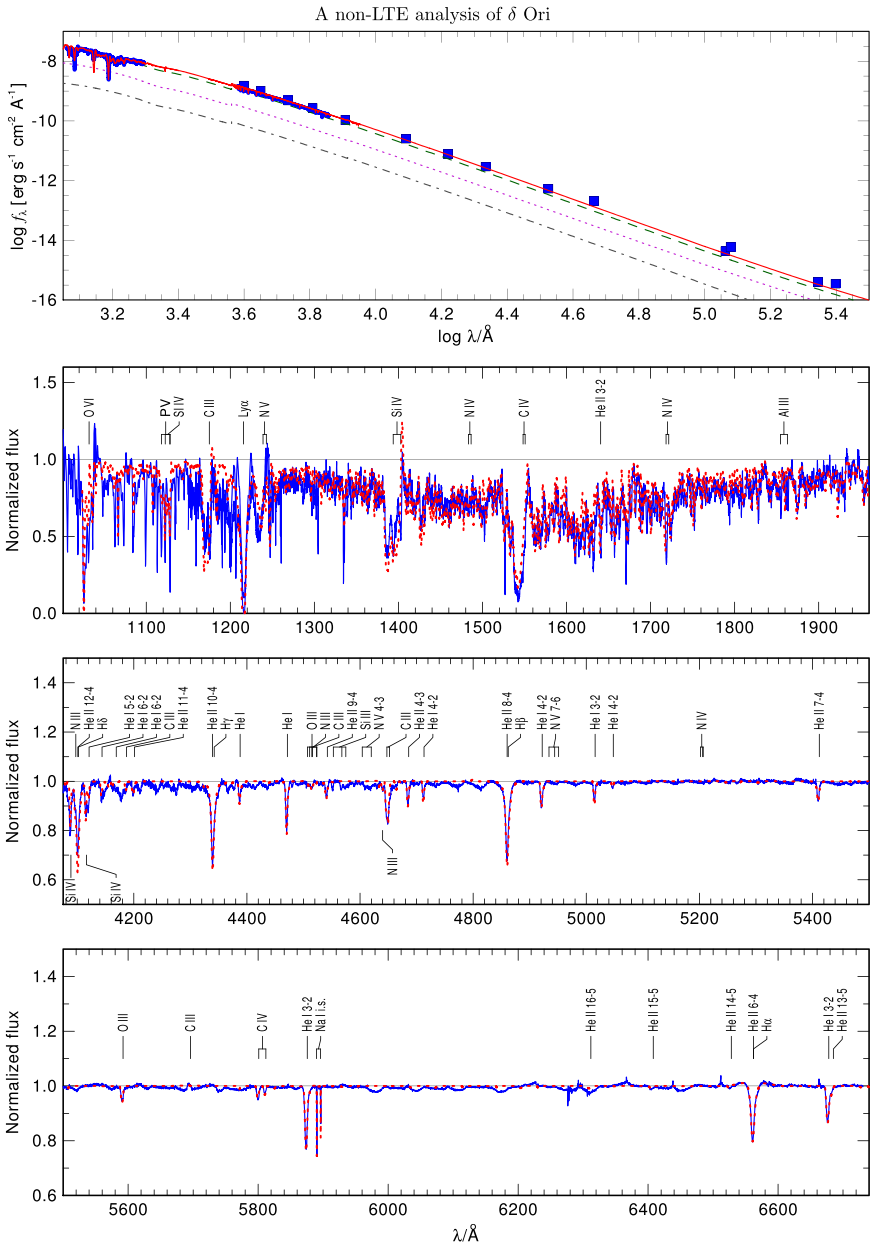

Figure 2. Upper panel: comparison between observations (blue squares and lines) and the total synthetic SED (red solid line), which consists of the primary (green dashed line), secondary (gray dash–dotted line), and tertiary (pink dotted line) models. Lower panels: comparison between the composite synthetic (red dotted line) and observed (blue line) normalized spectra in the UV and optical. Both spectra roughly correspond to phase $\phi = 0.54$. For clarity, we refrain from showing the contributions of each component model to the normalized spectrum. The wavy pattern seen in the observed spectrum (e.g., in ≈6000−6200 Å) is an artifact caused by connecting the echelle orders, not related to the stellar system.

to note that Sota et al. (2011) recently added the suffix "Nwk" to the spectral type of Aa1, implying relatively weak nitrogen lines, which we confirm independently.

For $d = 380$ pc, the distance-dependent parameters agree well with calibrations by Martins et al. (2005). Interpolating to luminosity class II, calibrations by Martins et al. (2005) imply $\log L/L_\odot = 5.3$, $M = 25\,M_\odot$, $R_{2/3} = 18.2\,R_\odot$, and $M_V = -5\overset{\mathrm{m}}{.}73$ for an O9.5 II star, which is consistent with our results. Furthermore, this distance implies radii and masses for the primary and secondary that agree well with the results obtained independently in Paper III. However, very peculiar values are obtained when using the *Hipparcos* distance of $d = 212$ pc (see lower part of Table 1). In fact, all three components appear to be peculiar when adopting the *Hipparcos* distance. While a membership in a close binary system offers some room for deviations from standard values, this would not explain why the distant tertiary Ab should be peculiar too. The fact that distance-independent parameters are not unusual raises even more suspicion regarding the *Hipparcos* distance.

A similar discrepancy is observed in other bright stars: Hummel et al. (2013) analyzed the binary system ζ Orionis A ($V = 1.79$) and inferred a distance of $d = 294 \pm 21$ pc based on an orbital analysis, and $d = 387 \pm 54$ pc based on a photometric estimate. Both of these distances are significantly larger than the corresponding *Hipparcos* distance of

$d = 225^{+38}_{-27}$ pc (van Leeuwen 2007), which encouraged them to discard the *Hipparcos* distance in their study. Another bright star for which the *Hipparcos* parallax implies very peculiar stellar parameters is the prototypical O supergiant ζ Puppis ($V = 2.25$). Its distance was suggested to be at least twice as large as implied by its measured parallax (Pauldrach et al. 2012; Howarth & Stevens 2014).

Returning to δ Ori A, our estimate of $d \sim 380$ pc would correspond to a parallax of $\pi \sim 2.6$ mas, deviating by $\sim 3.5\sigma$ from the newly reduced *Hipparcos* parallax of 4.71 ± 0.58 mas (van Leeuwen 2007). The probability for such a deviation to arise randomly is thus extremely small ($<0.1\%$). Ground-based parallaxes for δ Ori A generally suffer from much larger uncertainties. For example, the Yale catalog gives $\pi = 9.7 \pm 6.7$ mas (van Altena et al. 1995). It is interesting to note that the original *Hipparcos* catalog gives a parallax of 3.56 ± 0.83 mas (ESA 1997a, 1997b). In this case, the deviation could be plausibly explained as a random error, with 2.6 mas being $\sim 1\sigma$ away. While stellar multiplicity has been suggested to cause systematic errors in parallax measurements (e.g., Szabados 1997), the argument is unlikely to hold here given the different timescale of the involved orbits compared to that of the parallax measurement (which is to say, a year). However, large errors in the parallax measurement are also expected to occur in the case of very bright stars, which could lead to saturation, resulting in an inaccurate estimate of the barycenter of the point-spread function. Brightness is indeed a property δ Ori A shares with the objects mentioned above. It is beyond the scope of the paper to judge whether the new *Hipparcos* reduction suffers from underestimated errors, but the fact that several bright stars show a similar pattern should encourage thorough studies on the matter.

The distance to δ Orionis is difficult to directly measure with modern techniques. The system is probably too bright for ground-based (e.g., RECONS)[17] as well as space-based instruments (e.g., the *Hubble Space Telescope*'s Fine Guidance Sensor; the *Gaia* mission). Our best hope is to obtain the RV curve of the secondary, which requires optical spectroscopy with an S/N $\gtrsim 1000$ (Paper III). Then, with a direct measure of the system parameters, follow-up long-baseline interferometry may provide the angular extent of the orbit, allowing for an orbital parallax measurement similar to that of ζ Ori A (Hummel et al. 2013). At 380 pc, the angular extent of the orbit will be on the order of 0.5 mas and thus difficult to measure, as the smallest angular separation for a binary yet resolved is 1.225 mas (Raghavan et al. 2009). However, this was done in the K-band with the CHARA Array, so the resolution in the R band should be sufficient to resolve the binary. Moreover, along with a light-curve analysis, and possessing *both* RV curves, one could accurately derive the masses and radii of both components, which, upon comparison with a distance-dependent spectral analysis, would supply another constraint on the distance. For now, we suggest that the *Hipparcos* distance may be underestimated, but leave the question open for future studies to resolve.

4.2. Constraining the Parameters of Aa2 and Ab

The five columns of Figure 3 depict six prominent He II and He I lines, from left to right: He II λ4686, He I λ4922, He II λ5411, He I λ5876, and the two adjacent lines He I λ6678 and He II λ6683. Each row depicts a different orbital phase, from top to bottom: $\phi = 0.02$, 0.19, 0.38, 0.54, 0.84. This time, we explicitly show the relative contributions of the primary (green dashed line), secondary (gray solid line), and tertiary (pink dot–dashed line) to the total synthetic spectrum (red dotted line), compared to the observations at each phase (blue line). In Table 2, we specify the RVs with which the three components are shifted at each phase. The RVs for the primary were inferred in this study and agree very well with the RV curve of Mayer et al. (2010) and those of Paper III.

4.2.1. The Tertiary

There is a wide and shallow spectral feature that does not originate in the primary and is constant along all orbital phases (see Figures 3 and 4). Like Mayer et al. (2010), we identify this feature with the tertiary Ab, which is in fact the second brightest source in the system. The RV of the tertiary, which is practically constant over all phases, is also inferred independently, and agrees well with that suggested by Mayer et al. (2010).

We find that the tertiary contributes significantly more to H I lines than to He II lines. Together with the visual flux ratio implied from observations, this leads to a tertiary temperature of $T_* \sim 29.0$ kK. The gravity and mass-loss of the tertiary were constrained based on the Balmer lines. As already discussed, it is very hard to identify the explicit contribution of the tertiary to these lines, and so the gravity and mass-loss of the tertiary are only roughly constrained. The parameters derived for the tertiary (see Table 1) are consistent with it being a *B*0 IV-type star (Habets & Heintze 1981; Schmidt-Kaler 1982).

4.2.2. The Secondary

It is very hard, or perhaps impossible, to recognize any contribution from Aa2 to the spectrum. One exception might be the He I lines $\lambda\lambda$4026, 4144 at phase $\phi = 0.84$, which we show in the left and right panels of Figure 4, respectively (colors and lines are as in Figure 3). At this phase, the primary's RV approaches its maximum of ~ 110 km s^{-1}, and so the secondary is expected to be more easily observed. The He I λ4026 line, for example, seems to have an extended wing toward blueshifted wavelengths. The very weak He I λ4144 line is one of the few spectral lines that possibly portrays a partially isolated feature originating in the secondary. We therefore infer an RV for the secondary in this phase. For all other phases, we adopt the secondary's RVs from Harvin et al. (2002), since the secondary's lines cannot be isolated in the spectrum. However, as Mayer et al. (2010) pointed out, it is likely that Harvin et al. (2002) confused the secondary with the tertiary, so that the secondary RVs reported by Harvin et al. (2002) are questionable.

Even without directly detecting the secondary, we can still constrain its stellar parameters. Since the light curve provides a lower limit for its visual flux (see Section 3.3), the luminosity of Aa2 cannot be arbitrarily small. Instead, to avoid too-strong line features from the secondary (which are not observed), we are forced to change other stellar parameters, e.g., T_* and $v \sin i$. The secondary's projected rotation velocity ($v \sin i \approx 150$ km s^{-1}) agrees with the feature shown in the right panel of Figure 4, and the secondary temperature ($T \approx 26$ kK) is consistent with that obtained from the light curve analysis of the system (Paper III).

In Section 3.3, we argued that the light curve of δ Ori Aa implies that the secondary contributes at least 5.4% to total

[17] www.recons.org

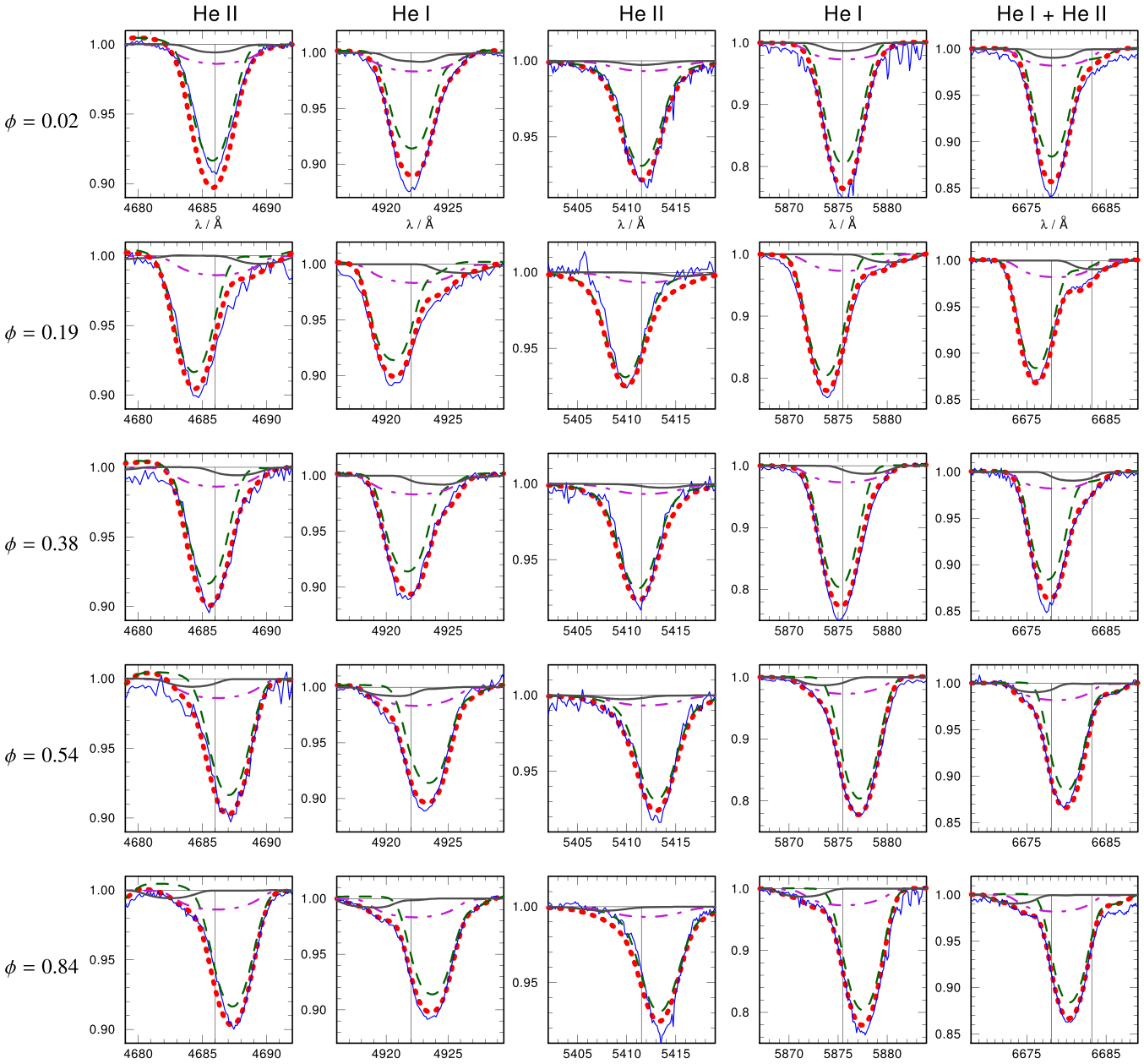

Figure 3. Twenty-five panels show the contribution of the primary (green dashed line), secondary (gray solid line), and tertiary (pink dash–dotted line) models to the composite synthetic spectrum (red dotted line) for six prominent helium lines and five different phases, compared with observations (blue line). The lines depicted are, from left to right, He II λ4686, He I λ4922, He II λ5411, He I λ5876, and the two adjacent lines He I λ6678 and He II λ6683. The phases are, from top to bottom, ϕ = 0.02, 0.19, 0.38, 0.54, and 0.84. At each phase, the component models are shifted with the velocities given in Table 2.

Table 2
Radial Velocities Derived/adopted for each Phase in km s^{-1}

Phase	Aa1[a]	Aa2[b]	Ab[a]
0.02	0	10	25
0.19	−92	230	25
0.38	−22	120	25
0.54	83	−100	25
0.84	105	−210	25

Notes.
[a] Values for primary and tertiary derived in the analysis.
[b] Values for secondary adopted from Harvin et al. (2002), with the exception of phase 0.84, which is derived here.

visual flux of the system. In this section, we argue that the secondary can contribute no more than this amount. In other words, our lower bound for the relative flux contribution becomes also our upper bound, and therefore $\Delta V_{\rm Aa1Aa2} \approx 2\overset{\rm m}{.}8$. Together with the temperature of the secondary, this enables us to infer an approximate value for the luminosity of the secondary. Its parameters suggest it is a $\approx$ B1 V type star (Habets & Heintze 1981; Schmidt-Kaler 1982).

4.3. Bulk and Turbulent Motions

4.3.1. Rotation and Macroturbulence

Rotation is usually the dominant broadening mechanism of photospheric metal lines in OB type spectra, as is the case here.

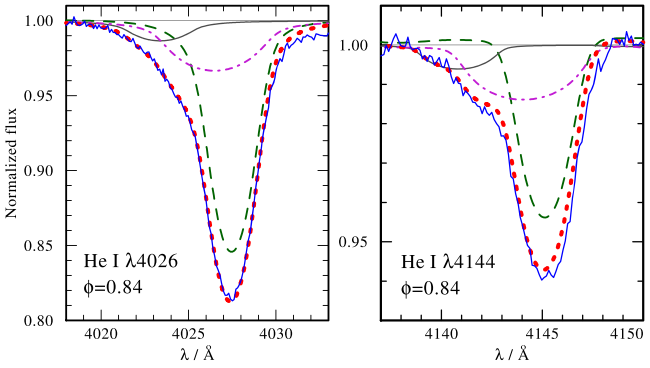

Figure 4. Two panels depict two observed He I lines (blue lines) at phase $\phi = 0.84$ in which the secondary may be detectable. The different curves correspond to the primary (green dashed line), secondary (gray solid line), tertiary (pink dash–dotted line), and total (red dotted line) synthetic spectra.

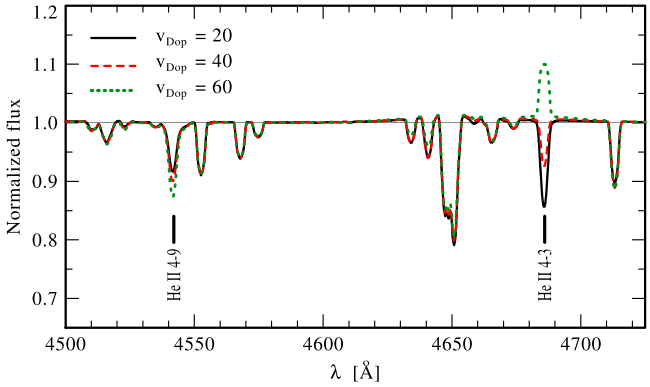

Figure 5. Illustration of the extreme sensitivity of the He II λ4686 line to the parameter v_{Dop}. Here we depict only the primary model, calculated with the parameters in Table 1, but with $v_{Dop} = 20$ km s^{-1} (black solid line), 40 km s^{-1} (red dashed line), and 60 km s^{-1} (green dotted line). The formal integration is performed with the same turbulent velocity as given in Table 1. Notice that most lines hardly react to this parameter.

We infer the projected rotational velocity $v \sin i$ by convolving the synthetic spectrum with a rotation profile and comparing the line shapes to the observed spectrum. While flux convolution is a fair approximation for photospheric spectra, it does not account for the effect of limb darkening and for the extended formation regions of some lines. Accounting for rotation in the formal integration is essential for a consistent inclusion of these effects, but is computationally expensive. We therefore use the convolution method to infer $v \sin i$, and, only after obtaining the best-fit value of $v \sin i$, do we account for rotation directly in the formal integration (see Hillier et al. 2012; Shenar et al. 2014), assuming co-rotation up of the photosphere ($\tau_{Ross} = 2/3$) and angular momentum conservation in the wind. Compared to simple flux convolution, the detailed treatment of rotation generally yields deeper lines with less elliptic profiles (e.g., Unsöld 1955) and may significantly affect the inferred abundances, projected rotation velocities, and even fundamental stellar parameters.

The effect of rotation on the spectrum is coupled to the effects of macroturbulence v_{mac}, which we model using a Radial–Tangential profile (Gray 1975; Simón-Díaz & Herrero 2007). Macroturbulence does not enter the radiative transfer per definition. Therefore, like solid body rotation, macroturbulence conserves the EWs of the lines. Typical values of $v_{mac} \sim 50$ km s^{-1} are reported for OB-type stars (Lefever et al. 2007; Markova & Puls 2008; Bouret et al. 2012). While the origin of macroturbulence is not certain, it has been suggested to be a manifestation of collective pulsational broadening (e.g., Aerts et al. 2009). $v \sin i$ and v_{mac} are inferred simultaneously from the profile shapes of helium lines and metal lines. Not accounting for macroturbulence generally results in qualitatively different profiles from what are observed in photospheric lines (see, e.g., example given by Puls et al. 2008).

Harvin et al. (2002) inferred $v \sin i = 157$ km s^{-1} for the primary. While this value agrees well with the wings of prominent helium and metal lines, it leads to too-broad Doppler cores. A significantly better fit is obtained with $v_{mac} = 60$ km s^{-1} and $v \sin i = 130$ km s^{-1}. For an inclination of $i = 76°$ (Paper III) and a radius of $R = 16.5\,R_{\odot}$ (Table 1), this could imply that the rotation period is approximately synchronized with the orbital period of 5.7 days.

For the tertiary, we find an optimal fit for $v \sin i = 220$ km s^{-1} and $v_{mac} = 50$ km s^{-1}, thus confirming the findings of Harvin et al. (2002) and Mayer et al. (2010) that the tertiary is a rapid rotator. For the secondary, motivated by the arguments discussed in Section 4.2, we estimate $v \sin i \sim 150$ km s^{-1}. We adopt $v_{mac} = 0$ for the secondary, lacking any spectral lines from which it can be inferred. Any other typical values would bear no effect on our results.

4.3.2. Microtubulence and Terminal Velocity

In contrast to macroturbulence, microscopic turbulent motion enters directly into the process of radiative transfer and generally affects the EWs of spectral lines. In the non-LTE iteration, we do not specify the microturbulence explicitly, but rather the total Doppler width v_{Dop} of the opacity and emissivity profiles. v_{Dop} thus determines the resolution of the frequency grid in the non-LTE iteration. This parameter generally has a negligible effect on the obtained population numbers, with the extreme exception of the He II λ4686 line. As was already noted by Evans et al. (2004), this line reacts very strongly to changes in v_{Dop}. We illustrate this in Figure 5, where we show a segment of the optical spectrum containing the He II λ4686 line. In the figure, we depict three models corresponding to the primary calculated with parameters identical to those given in Table 1, but with $v_{Dop} = 20$, 40, and 60 km s^{-1}, respectively. It is evident that the He II 4686 Å line reacts remarkably strongly to v_{Dop}. The exact origins of this effect are still under investigation (Shenar et al. 2015, in preparation), but likely involve a feedback effect in the highly nonlinear iterative solution of the radiative transfer problem. The remaining He II lines show a much weaker reaction in the opposite direction. Other lines hardly respond to changes of this parameter. This example shows that, overall, the choice of the parameter v_{Dop} is not critical for the fit, and that He II λ4686 is a poor temperature indicator. Based on this, $v_{Dop} = 30$ km s^{-1} is used in the analysis, consistent with the inferred microturbulence (see below).

In the formal integration, apart from including natural and pressure broadening, the Doppler width is separated into a thermal component v_{th}, which follows the temperature stratification in the model, and a depth-dependent microturbulence component $\xi(r)$, which is assumed to be identical for all ions. As described in Section 3.1, $\xi(r)$ is interpolated between

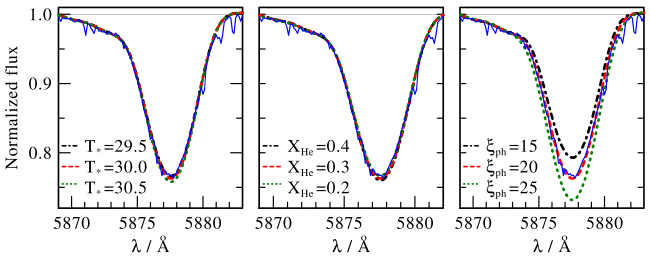

Figure 6. Sensitivity of the He I λ5876 line to temperature, helium abundance, and microturbulence. The observed spectrum (blue line) at phase $\phi = 0.84$ is plotted along with three composite synthetic spectra calculated with the parameters given in Table 1, but with different temperature (left panel: $T = 29.5$, 30, 30.5 kK), helium abundance (middle panel: $X_{\rm He} = 0.2$, 0.3, 0.4), and photospheric microturbulence (right panel: $\xi_{\rm ph} = 15$, 20, 25 km s^{-1}) for the primary model (black dot–dashed, red dashed, and green dotted lines, respectively).

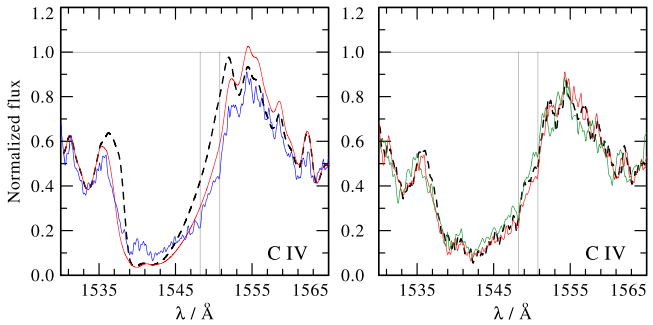

Figure 7. Left panel: observed C IV resonance doublet at phase $\phi = 0.73$ (blue line) is compared to two synthetic composite spectra, with increased wind turbulence of $\xi_{\rm w} = 200$ km s^{-1} in the primary model (red solid line), and without it (black dashed line). Large microturbulent velocities beyond the sonic point are the only mechanism that can reproduce the redshifted absorption trough. Note that a further improvement of the profile is achieved by accounting for macroclumps, which are not included here. Right panel: comparison of three *IUE* observations at phases $\phi = 0.18$, 0.73, 0.98 (black, red, and green lines, respectively), illustrating that the redshifted absorption trough is observed at all phases.

the photospheric $\xi_{\rm ph}$ and wind $\xi_{\rm w}$ turbulent velocities between two pre-specified radii, all of which are free parameters.

Values of photospheric microturbulence reported for O giants range between $\sim$10 km s^{-1} and 30 km s^{-1} (e.g., Gies & Lambert 1992; Smartt et al. 1997; Bouret et al. 2012). Since the photospheric microturbulence $\xi_{\rm ph}$ is rarely found to be larger than 30 km s^{-1}, its effect on the profile width is negligible compared to the effect of rotation. However, $\xi_{\rm ph}$ can have a very strong effect on the EW of spectral lines. The abundances are thus coupled to $\xi_{\rm ph}$, and wrong turbulence values can easily lead to a wrong estimation of the abundances (e.g., McErlean et al. 1998; Villamariz & Herrero 2000). To disentangle the abundances and turbulence from, e.g., the temperature, we take advantage of the fact that different lines respond individually to changes in abundances, turbulence, and temperature, depending on their formation process. Figure 6 shows an example. The left, middle, and right panels depict the He I λ5876 line as observed at phase $\phi = 0.84$ (blue line). In each panel, we show three different composite synthetic spectra (i.e., composing all three components), which were calculated with parameters identical to those given in Table 1, except for one stellar parameter of the primary. In the left panel, T_* is set to 29.5, 30, and 30.5 kK. In the middle panel, the helium mass fraction is set to $X_{\rm He}$ of 0.2, 0.3, and 0.4. Lastly, in the right-most panel, we set $\xi_{\rm ph}$ to 15, 20, and 25 km s^{-1}, respectively. The three composite spectra at the left and middle panels can hardly be distinguished from each other, portraying the insensitivity of the He I λ5876 line to temperature and helium abundance. In the relevant parameter domain, it is mainly $\xi_{\rm ph}$ which influences the strength of the He I λ5878 line. By considering hundreds of lines at all available orbital phases, we find that $\xi_{\rm ph} = 20$ km s^{-1} provides the best results for the primary's model. Similarly, we find that a microturbulence of 10 km s^{-1} for the tertiary yields the best global fit.

We find evidence for a rapid increase of the turbulent velocity in the primary right beyond the sonic point. The left panel of Figure 7 shows the C IV $\lambda\lambda$ 1548, 1551 resonance doublet, as observed in the *IUE* spectrum taken at phase $\phi = 0.73$. The observation shows a wide absorption trough which extends to redshifted wavelengths, and our task is to reproduce this feature. The black dashed line depicts the composite synthetic spectrum calculated with the parameters in Table 1, but without an increased wind turbulence in the primary model, i.e., $\xi_{\rm w} = \xi_{\rm ph} = 20$ km s^{-1}. The absorption trough is not reproduced. Increasing the terminal velocity only affects the blue edge of the line. Varying β in the domain 0.7–1.5 does not lead to any notable changes in the spectrum. The only mechanism that is found to reproduce the redshifted absorption trough is a rapid increase of the microturbulence beyond the sonic point. The red solid line was calculated like the dashed black line, but with a wind turbulent velocity of $\xi_{\rm w} = 200$ km s^{-1}. $\xi(r)$ is assumed to grow from $\xi_{\rm ph}$ at $r_{\rm in} \leqslant 1.1\,R_*$ to $\xi_{\rm w}$ at $r_{\rm out} \geqslant 2\,R_*$. At the same time, the blue absorption edge is shifted by $\sim$200 km s^{-1}, thus influencing the value deduced for v_∞. The right panel of Figure 7 shows the same C IV resonance doublet, as observed in three *IUE* spectra taken at phases $\phi = 0.18$, 0.72, 0.98 (black, red, and green lines, respectively). The figure illustrates the relatively small variability of this line, showing that our results do not depend on phase, and rejecting the contamination by another component as an explanation for the extended redshifted absorption. The absorption trough is not reproduced for $r_{\rm out}$ significantly larger than $2\,R_*$, which is understandable given the need for redshifted absorption. It is interesting to note that it is microturbulence, and not macroturbulence, that is needed to reproduce this feature. A further improvement of the line profile fit is obtained by accounting for optically thick clumps (macroclumps) in the wind, as we will discuss in Section 5. We do not include macroclumping at this stage in order to single out the effect of $\xi_{\rm w}$ on the line profile.

Having inferred the turbulent velocity and after accounting for clumping in the wind of the primary, it is straight-forward to derive the terminal velocity v_∞ from resonance P Cygni lines. All prominent lines in the UV imply the same value for v_∞ (2000 ± 100 km s^{-1}).

4.4. Uncertainties

Since the calculation of a PoWR model atmosphere is computationally expensive, a statistical approach for error determination is virtually impossible. The errors given in Table 1 for each physical quantity are obtained by fixing all parameters but one and varying this parameter, estimating upper and lower limits that significantly change the quality of the fit in many prominent lines relative to the available S/N. Errors for parameters that are implied from fundamental

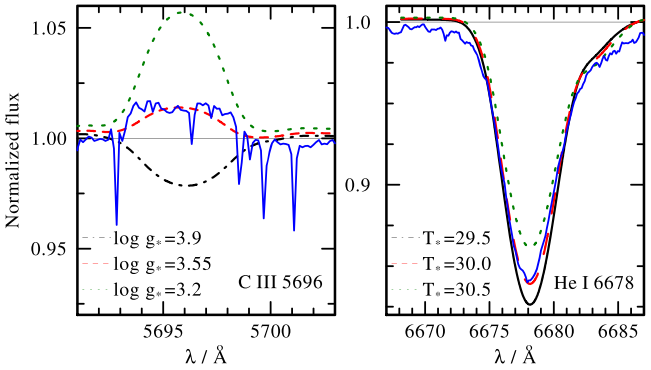

Figure 8. Left panel: sensitivity of C III λ5696 to gravity. The observed spectrum at phase $\phi = 0.02$ (blue line) is compared to three composite synthetic spectra calculated with the parameters given in Table 1, but with $\log g_*$ of the primary set to 3.9, 3.55, and 3.2 (black dot–dashed, red dashed, and green dotted lines, respectively). Right panel: sensitivity of He I λ6678 to temperature. We set the temperature of the primary to 29.5, 30.0, and 30.5 kK (black dot–dashed, red dashed, and green dotted lines, respectively).

parameters via analytical relations, e.g., the spectroscopic mass, are calculated by means of error propagation. In the case of multiple systems, all models but one test model are kept fixed, and only one parameter of the test model is varied.

As mentioned in Section 4, it is very hard to constrain the gravity of the primary due to contamination by the other components. However, we took advantage of the fact that specific lines do drastically change their strength as a function of gravity. An example of such a diagnostic line, C III λ5696, is shown in the left panel of Figure 8, as observed at phase $\phi = 0.02$ (blue line). Three composite spectra (i.e., including all components) are plotted, where only the $\log g_*$ of the primary is changed to 3.9 (black dot–dashed line), 3.55 (red dashed line), and 3.2 (g cm^{-2}) (green dotted line). The remaining stellar parameters are kept fixed to the values given in Table 1. This line only starts to portray emission when $\log g_* \sim 3.5$ (g cm^{-2}). This line also serves as a good example of why χ^2 fitting would not always suggest the best fitting model. The contribution of such a small line to the reduced χ^2 is negligible, unlike its diagnostic power. The right panel of Figure 8 depicts the sensitivity of the He I line to the stellar temperature. The temperature of the primary is changed to 29.5 (black dot–dashed line), 30 (red dashed line), and 30.5 kK (green dotted line). Most He I and He II lines react strongly to changes in the temperature and thus enable us to sharply constrain it.

5. INHOMOGENEITIES IN THE PRIMARY'S WIND

Evidence for wind inhomogeneities (clumping) in the winds of hot stars are frequently reported. Hillier (1984) and Hillier (1991) illustrated the effect of optically thin clumps on the electron scattering wings of Wolf–Rayet emission lines. More compelling direct evidence for clumping in the form of stochastic variability on short timescales was observed in both Wolf–Rayet (e.g., Lépine & Moffat 1999) and OB stars (Eversberg et al. 1998; Markova et al. 2005; Prinja & Massa 2010). Clump sizes likely follow a continuous distribution (e.g., power law), which is intimately connected with the turbulence prevailing in the wind (e.g., Moffat 1994). However, since consistent non-LTE modeling of inhomogeneous

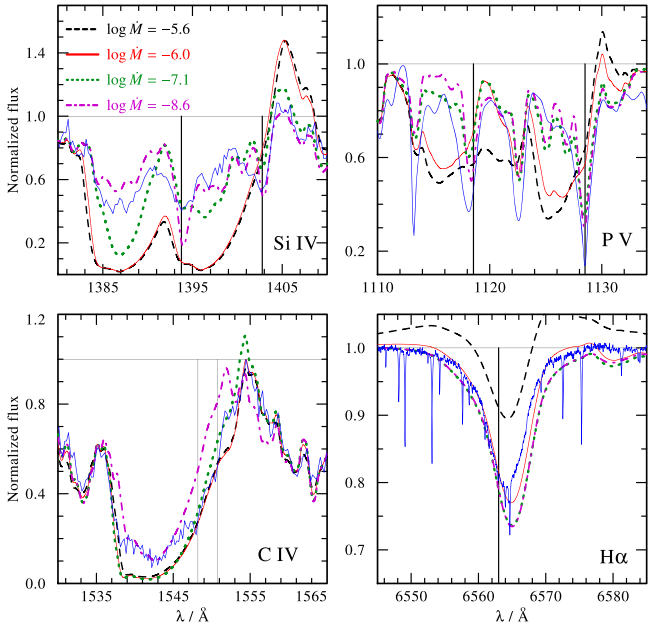

Figure 9. Observed "wind" lines (blue line): the Si IV $\lambda\lambda$1394, 1408 (upper left), C IV $\lambda\lambda$1548, 1551 (lower left), and P V $\lambda\lambda$1118, 1128 (upper right) resonance doublets, and Hα (lower right), roughly at phase $\phi \sim 0.8$, except for the Copernicus data (P V), which are co-added. Each panel depicts four composite spectra with the same parameters as in Table 1, but without clumping ($D = 1$), and with different mass-loss rates: $\log \dot{M} = -5.6$, -6.0, -7.1, and $-$x8.6 ($M_\odot$ yr^{-1}) (black dashed, red solid, green dotted, and purple dash–dotted lines, respectively). The Hα and different P Cygni lines clearly imply different mass-loss rates, and cannot be fitted simultaneously.

stellar winds in 3D is still beyond reach, the treatment of clumping is limited to approximate approaches.

5.1. Microclumping

A systematic treatment of optically thin clumps was introduced by Hillier (1984) and later by Hamann & Koesterke (1998) using the so-called microclumping approach, where the population numbers are calculated in clumps that are a factor of D denser than the equivalent smooth wind. In this approach, processes sensitive to ρ, such as resonance and electron scattering, are not sensitive to clumping, and imply $\dot{M}$ directly. However, processes that are sensitive to ρ^2, such as recombination and free–free emission, are affected by clumping, and in fact only imply the value of $\dot{M}\sqrt{D}$. This enables consistent mass-loss estimations from both types of processes, and offers a method to quantify the degree of inhomogeneity in the wind in the optically thin limit.

To investigate wind inhomogeneities in the primary Aa1, we first adopt a smooth model. The four panels of Figure 9 depict four "wind" lines: three UV resonance doublets belonging to Si IV, P V, and C IV ($\propto\rho$), and Hα, as the only recombination line potentially showing signs for emission ($\propto\rho^2$). In each of the four panels, four composite synthetic spectra (i.e., containing all three components) are plotted along the observation (blue line). The four models differ only in the mass-loss rate of Aa1: $\log \dot{M} = -5.6$ (black dashed line), -6.0 (red solid line), -7.1 (green dotted line), and -8.6 ($M_\odot$ yr^{-1}) (purple dot–dashed line). The remaining stellar parameters are identical to the ones given in Table 1 (for $d = 380$ pc), but with $D = 1$ for the primary. The observations roughly

correspond to phase $\phi \sim 0.8$, except in the case of the P v doublet, which is obtained from the co-added *Copernicus* data (see Section 2).

While a best fit for Hα (lower right panel in Figure 9) is obtained with $\log \dot{M} \approx -6.0\,(M_\odot\ \mathrm{yr}^{-1})$, we note that H$\alpha$ portrays noticeable variability with time, which increases the uncertainty of the inferred mass-loss rate. Furthermore, our estimation of the mass-loss rate from Hα could be inaccurate due to underestimated contribution to the emission by either the tertiary or by the wind–wind collision effect. Fortunately, the Hα mass-loss rate is supported by radio observations. Assuming a smooth wind, Lamers & Leitherer (1993) infer a mass-loss rate of $\log \dot{M} \approx -5.95\,(M_\odot\ \mathrm{yr}^{-1})$ based on the radio flux of the system for an adopted distance of $d = 500$ pc. This value is revised to $\log \dot{M} \approx -6.1\,(M_\odot\ \mathrm{yr}^{-1})$ for $d = 380$ pc, only slightly smaller than the value derived for Hα in this study. Since both of these processes scale as ρ^2, and since the wind is assumed to be smooth in both cases, we therefore conclude that $\log\left(\dot{M}\sqrt{D}\right) \approx -6.0\,(M_\odot\ \mathrm{yr}^{-1})$ for the primary.

We now turn to the UV resonance lines. The Si IV line, shown in the upper left panel of Figure 9, is clearly not saturated in the observation. In the model, it remains saturated for $\log \dot{M} \geqslant -6.8\,(M_\odot\ \mathrm{yr}^{-1})$. A best fit is obtained with $\log \dot{M} \approx -7.5\ (M_\odot\ \mathrm{yr}^{-1})$. Together with the condition discussed in the previous paragraph, this implies $D \geqslant 40$; a best fit is obtained for $D \sim 1000$. The P v resonance line (upper right panel) implies a similar mass-loss rate, and hence a similar clumping contrast. The C IV line (bottom left panel), which does not look saturated in the observation,[18] requires a much lower mass-loss rate, of the order of $\log \dot{M} \approx -8.0\,(M_\odot\ \mathrm{yr}^{-1})$, and as a consequence implies $D \approx 10^4$.

However, are such large density contrasts physically sound? 1D and 2D time-dependent hydrodynamic simulations of line-driven winds suggest typical values of $D = 4-10$, with $D = 20-100$ occurring in the most extreme cases (Owocki et al. 1988; Feldmeier et al. 1997; Runacres & Owocki 2002; Sundqvist & Owocki 2013). Evolutionary considerations support $D \sim 2-3$ in order to obtain sufficient mass-loss from OB-type stars (e.g., Hirschi 2008). Values of 4–10 are typically reported for Wolf–Rayet stars based on electron scattering wings of strong emission lines (e.g., Todt et al. 2013; Hainich et al. 2014), while larger density contrasts of the order of 20 or more are suggested for OB stars (e.g., Bouret et al. 2012) to reconcile the strong discrepancy between $\dot{M}$ values derived from P Cygni resonance lines and recombination lines. Simultaneous analyses of the P v resonance doublet and optical recombination lines (e.g., Fullerton et al. 2006) may imply clumping factors as large as 100. However, we note that the latter authors neglect the effect of porosity (Oskinova et al. 2007), and that the resulting low mass-loss rates are inconsistent with polarization studies based on electron scattering (St-Louis & Moffat 2008), which depends linearly on density. It seems therefore that the implied values for D exceed plausible limits, and that no single value for D can satisfy all emission features simultaneously.

[18] We note that the *IUE* observation may suffer from calibration problems, which sheds doubt on whether the C IV resonance line is unsaturated. However, the observed shape of its absorption trough suggests that it is indeed unsaturated. This is evident in each of the 60 available *IUE* spectra, some even showing this more extremely. While we speculate that the line is desaturated here, our results do not depend on this strongly.

One possibility is that the abundances, or any other fundamental parameters derived for Aa1, which may affect the formation of the UV resonance lines, are significantly inaccurate. This is unlikely, because the photospheric features, as well as the general shape of the UV iron forest, are well reproduced and do not leave room for variations. Another possibility is that one of the components, perhaps through interaction with the primary's wind, is contaminating the observation. However, there are no clear indications for a periodic variation of the UV resonance lines with phase, as could be expected in such a case. We therefore suggest that not only is the wind of Aa1 clumped, but also that the clumps are optically thick in the strong UV lines. As illustrated by Oskinova et al. (2007), the optical thickness of the clumps leads to an effective reduction of the opacity of strong UV resonance lines, and could thus enable us to obtain results that are consistent over the X-ray, UV, optical, IR, and radio regimes. A further indication for optically thick clumps comes from the variable EW ratio of the two Si IV components. A ratio of 1 is expected to occur in the extreme case where the porous wind consists of optically thick clumps and "holes" between them, while a ratio of $\approx$2 (corresponding to the ratio of oscillator strengths of the two components) should occur in the case of a homogenous wind. The EW ratio of the Si IV doublet, which is observed to be smaller than 2, could be explained by the presence of optically thick structures present in the wind (see Prinja & Massa 2010).

5.2. Macroclumping

In PoWR, macroclumping is implemented only in the formal integration, leading to an effective reduction of the opacity in strong lines. Oskinova et al. (2007) thoroughly discuss the method, and illustrate the significant effect of macroclumping in the O supergiant ζ Puppis. Šurlan et al. (2013) model the effect of macroclumps by means of 3D Monte Carlo simulations and obtain similar results. A consequence of accounting for macroclumps is the need to introduce a further parameter, L_{mac}, which specifies the separation between the clumps. The non-LTE nature of the line formation makes a simultaneous prediction of L_{mac}, D and $\dot{M}$ practically impossible. We are therefore forced to adopt a value for one of these parameters. Since not much is known about the geometry of the clumps, we avoid prespecifying L_{mac}. Instead, we choose to adopt $D = 10$ as a compromise between $D \sim 2$ and $D \sim 100$. Motivated by hydrodynamic studies (Feldmeier et al. 1997; Runacres & Owocki 2002), we assume that the clumping initiates at $r = 1.1\,R_*$ and grows to its maximum contrast of $D = 10$ at $r \sim 10\,R_*$. Our results depend only weakly on the depth-dependence of $D(r)$.

Figure 10 portrays the two C IV and Si IV resonance doublets as observed at phase $\phi = 0.83$ (blue line). The black dashed line depicts the synthetic composite spectrum without the inclusion of macroclumping in the primary. The red dotted line depicts the same composite spectrum, but with $L_{\mathrm{mac}} = 0.5\,R_*$ adopted for the primary. The strong effect of macroclumping on the resonance lines is evident. The *H*α line, as well as the photospheric features, are hardly affected by the macroclumping formalism. The value $L_{\mathrm{mac}} = 0.5\,R_*$ provides a fair compromise for most wind lines, but the Si IV resonance lines in fact require larger values of the order of $L_{\mathrm{mac}} \sim R_*$. The analysis therefore suggests $L \gtrsim 0.5\,R_*$. This value should not be given too much significance, as macroclumps are treated

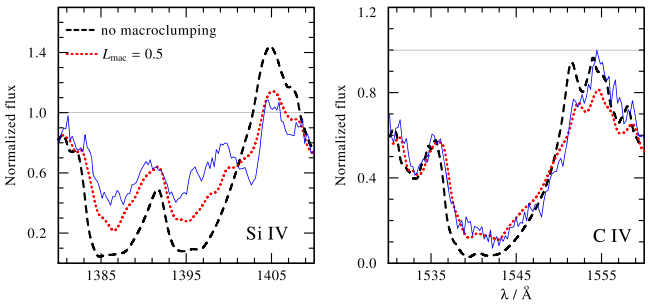

Figure 10. Observed Si IV and C IV resonance doublets (left and right panels, respectively) at phase $\phi = 0.83$ (blue line) compared to the composite synthetic spectrum calculated with the parameters in Table 1, but without macroclumping in the primary (black dashed line), and with macroclumping using $L_{mac} = 0.5\,R_*$ (dotted red line).

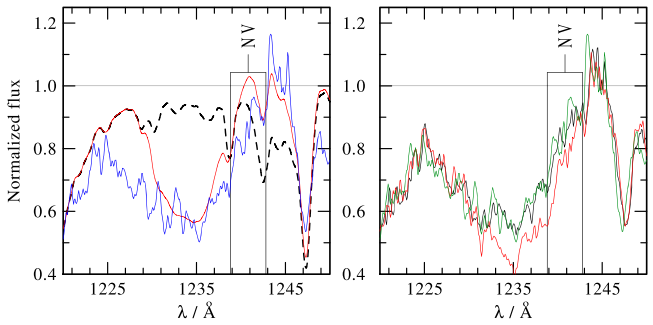

Figure 11. Left panel: observed N V resonance doublet at phase $\phi \sim 0.1$ (blue line) with two synthetic composite spectra, calculated with the parameters in Table 1, not including X-rays (black dashed line), and including X-rays (red solid line). Right panel: like the right panel of Figure 7, the three *IUE* observations at phases $\phi = 0.8, 0.3, 0.1$ (black, red, and green lines, respectively).

only as a rough approximation here. Nevertheless, we accounted for the major effects expected to rise from both optically thick and optically thin clumps, so mass-loss rates are unlikely to be very different than those derived here. Future variability studies should help to further constrain the amount of inhomogeniety in the primary's wind.

After assuming a clumping factor, the mass-loss rate is fairly well constrained, but still depends on the adopted distance. For the adopted distance of $d = 380$ pc, the mass-loss rate is found to be $\log \dot{M} = -6.4 \pm 0.15\,(M_\odot\ \mathrm{yr}^{-1})$. Since the mass-loss rate scales as $D^{-1/2}$, we can consider the two extreme alternatives for the clumping factor $3 \leqslant D \leqslant 50$ to set lower and upper bounds for the mass-loss rate of the primary: $-6.2 \leqslant \log \dot{M}_1 \leqslant -6.8\,(M_\odot\ \mathrm{yr}^{-1})$. Interestingly, Vink et al. (2000) predict $\dot{M}_{\mathrm{Vink}} = -6.48\,(M_\odot\ \mathrm{yr}^{-1})$ for a star with the parameters of the primary (for $d = 380$ pc) based on hydrodynamic calculations, which is in very good agreement with our results for the adopted clumping factor of $D = 10$ (see Table 1). However, we note that Vink et al. (2000) performed their calculations for homogenous winds, and it is not clear whether their predictions would remain the same in the case of significant inhomogeneities (Muijres et al. 2011).

6. WHERE DO THE X-RAYS IN δ ORI A COME FROM?

So far, our analysis has focused on the "cool" stellar wind. However, the cool wind alone cannot account for the observed X-rays in δ Ori A. It is commonly believed that X-ray emission in single stars originates in the wind due to instability of the line-driving mechanism (e.g., Feldmeier et al. 1997) or via acoustic driving from subsurface convection (Cantiello et al. 2009). In binary systems, an excess of hard-X-ray flux may originate from wind–wind collisions (Williams et al. 1990; Corcoran 2003). In this section, we explore the properties of the "hot" X-ray producing component.

6.1. Auger Ionization

The presence of strong X-ray radiation in OB-type stars was hypothesized prior to the first direct X-ray observations in massive stars. Cassinelli & Olson (1979) were the first to suggest that the detection of UV resonance lines of high-ionization ions such as N V and O VI, which are observed in many O-type stars, may indicate that Auger ionization (Meitner 1922; Auger 1923) plays an important role in their formation. Auger ionization occurs when very energetic photons remove an electron of an inner shell (usually the K-shell), ultimately resulting in double ionization. The Auger effect on UV spectra has been frequently detected in studies of OB-type stars (e.g., Oskinova et al. 2011).

The effect of X-rays in the wind of the primary Aa1 is evident by merely inspecting its UV spectrum. The presence of the strong UV resonance doublets O VI $\lambda\lambda$1032, 1038 and N V $\lambda\lambda$1239, 1243 cannot be reproduced otherwise. Indeed, an X-ray luminosity of $\approx 1.4 \cdot 10^{32}$ erg s^{-1} is reported for δ Ori A (Paper I), which corresponds to $\sim 10^{-6.87}$ times the total bolometric luminosity of the system.[19] The question remains, however, as to the origin of the X-ray radiation observed.

There are several arguments that suggest that emission from wind–wind collisions do not dominate the X-ray flux in δ Ori A. Paper II reports a relatively weak variability of the X-ray flux, which they cannot tie with certainty to phased-locked variations, in particular, wind–wind collisions. The inferred value of $\log L_X/L_{\mathrm{Bol}} \sim -6.87$ is typical for OB-type stars (e.g., Pallavicini et al. 1981; Seward & Chlebowski 1982; Moffat et al. 2002; Oskinova 2005; Nazé 2009), and does not imply any excess X-ray radiation from strong wind–wind collisions. Lastly, the N V $\lambda\lambda$1239, 1243 resonance doublet, which clearly forms due to the X-ray radiation, is persistent throughout all available *IUE* spectra (see right panel of Figure 11 below). If most X-rays originated in a collision zone which irradiated only a part of the star (whose orientation relative to the observer depended on phase), then a larger variability could be anticipated. It therefore seems plausible to assume that the X-rays originate in the wind itself.

We model the effect of X-ray radiation as described by Baum et al. (1992). The X-ray emission is assumed to originate in optically thin filaments of shocked plasma embedded in the wind. The X-ray field is characterized by the temperature T_X of the shocked plasma and the radially constant filling factor X_{fill}, which describes the ratio of shocked to non-shocked plasma. The onset radius of shocked plasma is denoted by R_0. The X-ray emissivity $\eta_X(r)$ at each radial layer $r > R_0$ is proportional to ρ^2. In principle, the three parameters T_X, X_{fill}, and R_0 are chosen such that the observed X-ray SED (Huenemoerder 2015, private communication) is approximately reproduced by the synthetic X-ray SED emerging from the model, after accounting for interstellar extinction. Once the

[19] We use here the total bolometric luminosity because all components are OB-type stars and are thus expected to emit X-rays proportionally to their luminosities.

onset radius R_0 has been fixed, T_X and X_{fill} follow from the observed SED. Motivated by the f/i analysis and X-ray line modeling results (see Sections 6.3 and 6.2), we fix the onset radius to $R_0 = 1.1\,R_*$, leading to $T_X = 3$ MK and $X_{fill} = 0.1$. These are only rough approximations to the X-ray properties in the wind (see Paper I), used to reproduce the bulk of X-ray emission observed.

The left panel of Figure 11 shows the effect of including X-rays in the wind of the primary on the N v resonance doublet $\lambda\lambda$1239, 1243. The blue line depicts the *IUE* observation of this doublet at phase $\phi = 0.1$. The black dashed line plots the synthetic composite spectrum without the inclusion of X-rays. Since the temperature in the wind is far from being sufficient to populate the N v ground state, only photospheric absorption is obtained. The red solid line is obtained after the inclusion of X-rays. While the line shape is not accurately reproduced, it is clear that X-rays are required in order to reproduce the observed P Cygni N v resonance line. Note also that the line is blended with components of iron lines in the blue part, making a determination of its terminal width difficult. The right panel of Figure 11 depicts three *IUE* observations at phases $\phi \sim 0.8, 0.3, 0.1$. While the N v resonance doublet shows stronger variability than most other resonance lines, the P Cygni feature is persistent and clearly visible in all 60 available *IUE* spectra.

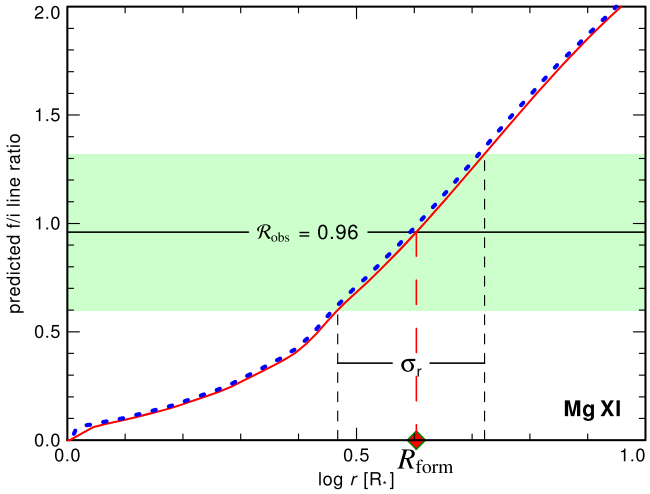

Figure 12. Theoretical f/i ratio $\mathcal{R}(r)$ is plotted as a function of the X-ray-formation radius (blue dotted line) for the Mg XI ion. The intersection of $\mathcal{R}(r)$ with the observed value $\mathcal{R}_{obs}$ implies the formation radius under the assumptions of the point-like approach. The error σ_r in the formation radius corresponds to 1σ measurement uncertainties in $\mathcal{R}_{obs}$, depicted by the green shaded rectangle. The red solid line depicts $\mathcal{R}(r)$ as well, but includes the contribution of collisions assuming a full ionization and a factor of 1000 density enhancement in the shocked plasma.

6.2. *f/i Analysis*

Spectra of He-like ions (i.e., ions with two electrons) exhibit a group of three neighboring X-ray lines referred to as resonance (r), forbidden (f), and intercombination (i) lines. A well-established method to constrain the formation region of X-rays in stellar winds makes use of observed forbidden-to-intercombination (f/i) line ratios. f/i analyses were originally developed to study the solar X-ray radiation (Gabriel & Jordan 1969; Blumenthal et al. 1972), but are now also frequently used to study the X-ray emission of OB and Wolf–Rayet stars (e.g., Waldron & Cassinelli 2001, 2007; Leutenegger et al. 2006). The f/i line ratio is determined by the relative population of the upper levels of the f and i lines, altered either by collisions or by photo-excitations (e.g., Porquet et al. 2001). For each helium-like ion, there are three possible transitions between the upper levels of the f and i lines, denoted in the following with indices $j = 0, 1, 2$. These transitions are typically at UV frequencies, although their exact wavelengths depend on the ion. The stronger the UV radiation field is, the smaller the f/i ratio becomes. A detailed treatment allows one to construct an equation that predicts the f/i line ratio $\mathcal{R}$ as a function of the radiative excitation rate ϕ and electron density n_e (see Blumenthal et al. 1972, Equation (1c)).

The interpretation of observed f/i line ratios requires some discussion. After all, what we observe is likely the X-ray radiation reaching us from an extended region where it is formed. The simplest way to interpret the observations would be to assume that the X-ray-emitting gas is distributed over a thin spherical shell located at a formation radius R_{form}, often referred to as the point-like interpretation. However, we know from detailed X-ray line fitting (see Section 6.3) that the X-ray radiation must originate in an extended region. Obviously, the point-like interpretation cannot describe the whole truth. A more generalized interpretation to the observed f/i line ratios, thoroughly described by Leutenegger et al. (2006), involves the integration of the X-ray radiation emanating from a continuous range of radii. Within the assumptions of this method, it is not the formation region that is sought, but the *onset* radius R_0 of the X-ray emission. We refer the reader to studies by Gabriel & Jordan (1969), Blumenthal et al. (1972), and Leutenegger et al. (2006) for a detailed description of the methodology of both interpretations.

We do not calculate the radiative excitation rate of the upper f level by diluting the photospheric fluxes (see Leutenegger et al. 2006, Equation (2)), but instead directly use the mean intensities J_ν at each radial layer, as obtained by our PoWR model. This way, we account for diffuse emission and limb darkening in a consistent manner. We include all three transitions, $j = 0, 1, 2$, in the calculation, properly weighted with their respective branching ratios. The relevant wavelengths λ_j and oscillator strengths f_j are extracted from the NIST database.

Figure 12 shows an example calculated for the He-like Mg XI ion. The blue dotted line depicts the f/i ratio $\mathcal{R}(r)$ predicted by the model for the point-like assumption as a function of the formation radius R_{form}, neglecting collisional excitation. The solid horizontal line depicts the observed value of $\mathcal{R}_{obs} = 0.96 \pm 0.36$ (Paper I). The shaded green area depicts the 1σ measurement uncertainty. If the major part of the X-ray radiation originates at one radial layer, this layer will be located at $R_{form} = 4.1^{+1.2}_{-1.0}\,R_*$, where the uncertainty σ_r corresponds to the measurement uncertainty. In Figure 12, we also illustrate the influence of collisional excitation on $\mathcal{R}(r)$. The red solid line also plots $\mathcal{R}(r)$, but accounts for collisional excitation, assuming a full ionization and an unrealistically large factor of 1000 for the density enhancement in the shocked regions. Evidently, the contribution of collisions to the excitation of the upper f level is negligible in δ Ori A.

In Figure 13, we compare the point-like interpretation with the more generalized interpretation described by Leutenegger et al. (2006) for the ion Mg XI. The red solid line depicts $\mathcal{R}(r)$, as in Figure 12. The green dashed line shows the predicted f/i

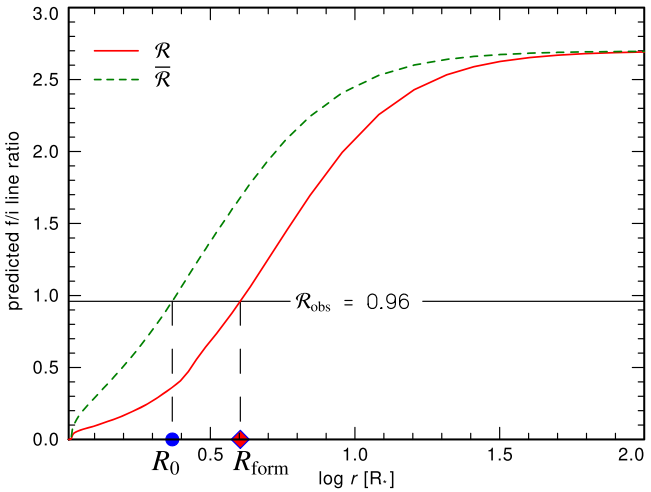

Figure 13. Same as Figure 12, but now accounting for an extended region of X-ray formation (green dashed line). The intersection of $\overline{\mathcal{R}}(r)$ with the observed value delivers the onset radius R_0.

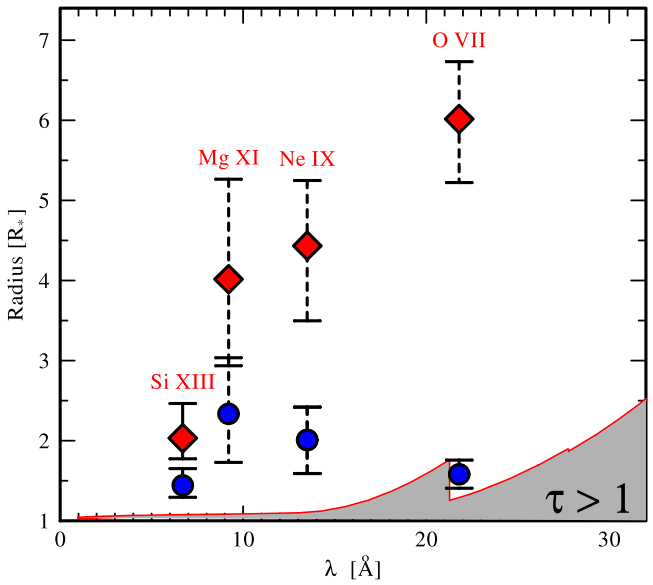

Figure 14. Inferred formation radii (red diamonds) and onset radii (blue circles) of the X-ray radiation, as inferred from the four He-like ions Si XIII, Mg XI, Ne IX, and O VII. The error bars correspond to measurement uncertainties propagated into errors of the inferred radii (see Figure 13). The shaded area corresponds to radii at which $\tau_{Ross} \geqslant 1$.

ratio $\overline{\mathcal{R}}(r)$ as a function of the *onset* radius R_0. Note that while both functions are depicted in the same coordinate frame, the meaning of r is different. As is evident from the figure, at the observed value of $\mathcal{R} = 0.96$, the onset radius R_0 predicted by integrating and weighting the contribution of all layers at $r > R_0$ is approximately 2.4 R_*.

Finally, Figure 14 graphically summarizes our results for the He-like ions Si XIII, Mg XI, Ne IX, and O VII using both the point-like and generalized interpretations. The measured f/i ratio of S XV does not provide any constraints, so this ion is not included. Measured f/i values and their uncertainties are given in Paper I. Formation radii inferred for each line are indicated with red diamonds, while onset radii are indicated with blue circles. The dashed vertical lines mark the $1-\sigma$ error range corresponding to f/i measurement uncertainties. The shaded gray area in both panels depicts the optically thick region in the model, i.e., regions where photons cannot escape.

Evidently, the X-ray formation radii are different for ions with significantly different ionization potentials (e.g., Si XIII versus O VII). This may suggest that a distribution of temperatures governs the formation radii (see, e.g., Krtička et al. 2009; Hervé et al. 2013). Figure 14 suggests that higher ions are formed at lower radii. This could imply that the hotter plasma is found closer to the stellar surface, while cooler plasma dominates farther out, a fact that was also pointed out by Waldron & Cassinelli (2007) from their study of a large sample of O-type X-ray spectra. The correlation between the ionization potential and location in the wind is no longer seen for the onset radii, which may suggest that X-rays are emitted in all He-like lines already very close to the stellar surface, independent of the element. This is in agreement with a picture based on hydrodynamic simulations, where plasma of different temperatures is present in cooling layers behind a shock front (Feldmeier et al. 1997). It is also worth noting that the formation radii roughly follow the same trend as the $\tau = 1$ surface of the cool wind, providing an independent confirmation that our analysis provides realistic values for the cool wind opacity.

6.3. X-Ray Line Modeling

We now demonstrate that the high-resolution X-ray spectrum of δ Ori A can be described consistently with the cool stellar wind model obtained from the analysis of UV and optical spectra. We use the high S/N X-ray spectra obtained by the *Chandra*'s HEG and MEG detectors. The observation consists of four different exposures taken at different orbital phases. A complete description of the X-ray observations and data analysis is given in Paper I. During the orbital motion, the RV of the primary changes between +114 and −78 km s^{-1}, with a systemic velocity of $\gamma = 15$ km s^{-1} (Paper III). It is ambiguous whether the observed X-ray Doppler shifts follow the expected orbital pattern (Paper II). Regardless, our tests show that the resulting Doppler shifts, which are comparable to the instrumental resolution and are much smaller than the wind velocity, bear a negligible effect on the modeled line profiles. We therefore neglect Doppler shifts due to orbital motion, and model the line profiles at the systemic velocity of 15 km s^{-1}. For all Lα lines of H-like ions, both components of the doublet are taken into account in the model.

We analyze the X-ray spectra by simulating X-ray lines using our 2D stochastic stellar wind code (Oskinova et al. 2004) and comparing them with observed lines. Because we are interested in the line profiles, the maximum of the synthetic lines is normalized to their observed maximum. Our model is based on the assumption of a two component medium: the "cool wind" and the "hot wind." The X-ray radiation is assumed to originate in optically thin filaments evenly distributed in the hot wind component (the treatment of resonant scattering in X-ray lines is presented in Ignace & Gayley 2002). The emissivity η_X scales as ρ^2, and the filling factor is assumed to be radially constant. A more sophisticated assumption on the behavior of η_X could lead to slightly different results numerically, but should not affect our conclusions qualitatively. The X-rays are attenuated on their way to the observer due to K-shell absorption in the cool wind.

Hence the X-ray propagation in the stellar wind is described by a pure absorption case of radiative transfer and is therefore relatively simple (e.g., Ignace 2001; Oskinova et al. 2004).

Macfarlane et al. (1991) demonstrated that the shape of optically thin emission lines is sensitive to the column density of the cool absorbing material: the lines become more skewed to the blue when the cool wind column density is large. They suggested using this property to measure the cool wind density. However, in clumped winds, the wind column density is reduced (Feldmeier et al. 2003), implying that the analysis of observed X-ray emission line profiles in O-type stars should account for wind clumping.

Several previous studies of X-ray emission lines in the spectra of O-type stars reported that accounting for wind clumping in the models does not improve the quality of the fit to the X-ray spectrum (e.g., Hervé et al. 2013). This is likely due to a degeneracy between the effects of mass loss and clumping on the X-ray spectrum: one can always neglect clumping, albeit at the cost of lower estimated wind opacity. However, as we show here, the effect of clumping cannot be assumed to be negligible for the realistic mass-loss rate derived from the detailed analysis of the cool wind.

In this study, we extract the mass-absorption coefficient $\kappa_\lambda(r)$ directly from the PoWR model of the primary's cool wind. Importantly, our models include clumping and the feedback of X-ray radiation on the ionization structure of the wind and are therefore consistent. We make a simplifying assumption that the velocity field of the hot X-ray-emitting plasma is the same as that of the cool X-ray-absorbing wind. Thus, with the exception of the radial distribution of the hot plasma, all X-ray model parameters are determined by the non-LTE stellar atmosphere model.

The theory of X-ray transfer in clumped stellar winds was developed by Feldmeier et al. (2003) and Oskinova et al. (2004). The special case of spherical clumps was considered by Owocki & Cohen (2006). The macroclumping formalism does not make any ad hoc assumptions about the size and optical depths of the cool wind clumps and is therefore suitable for effectively describing both smooth winds as well as clumped winds. This formalism further allows one to treat angle-dependent opacities, e.g., non-spherical wind clumps. A key parameter of the macroclumping formalism is the *fragmentation frequency* n_0 (s^{-1})—the number of clumps per unit time passing through a sphere at an arbitrary radius, which does not depend on the radius due to the assumption of clump conservation. n_0 is approximately related to the average separation between clumps $L_{\rm mac}$ (see Section 5) via $L_{\rm mac}^3 \approx R_*^2 v_\infty n_0^{-1}$. Allowing for an angular-dependent opacity, e.g., flattened clumps or shell fragments, results in distinct line shapes, with flat topped line profiles in the limiting case of opaque clumps (see also Ignace et al. 2012). For each line, we consider a smooth model and a clumped model with anisotropic wind opacity (see Oskinova et al. 2004), assuming flattened, "pancake-like" clumps (Lépine & Moffat 1999). Comparing the observations with a grid of inhomogenious models, we find that $n_0 = 8.6 \times 10^{-5}$ s^{-1} provides a good compromise for several X-ray lines. This roughly corresponds to a wind flow time of $t_{\rm flow} = R_*/v_\infty \approx 1.5$ hr ($n_0 \approx t_{\rm flow}^{-1}$), and to $L_{\rm mac} \sim 1\,R_*$, consistent with the lower bound $L_{\rm mac} \gtrsim 0.5$ implied from the UV and optical analysis.

The cool wind is virtually transparent at wavelengths shorter than 10 Å (see Figure 14 in Section 6.2). In this case, the line shape can provide vital information regarding the velocity field and density distribution of the hot plasma. The left panel of Figure 15 shows the observed Mg XII line compared with a smooth-wind model (blue dotted line) and a clumped-wind model (red solid line). The Mg XII line has the highest S/N in the HEG wavelength range, and since the HEG has a superior spectral resolution (0.012 Å) compared to the MEG (0.023 Å), it is especially useful for studying the detailed shape of line profiles. Figure 15 illustrates the above statement: lines at $\lambda \lesssim 10$ Å are hardly absorbed in the wind, and thus do not show any sensitivity to wind clumping. Furthermore, the good agreement between the models and the observations implies that the majority of X-rays originate in filaments co-moving with the cold wind, exhibiting the whole range of velocities up to roughly the terminal velocity in their line profiles.

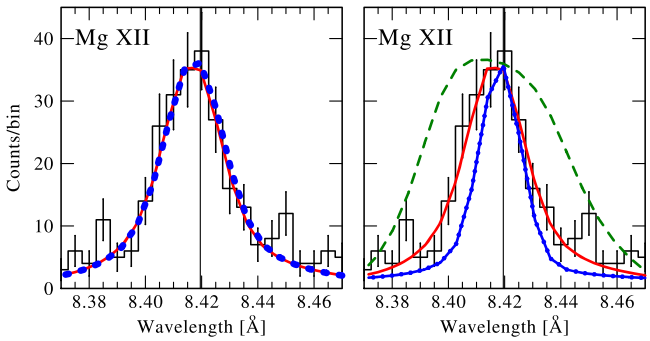

Figure 15. Left panel: observed co-added HEG±1 spectrum of δ Ori A centered on the Mg XII line (histogram), compared with a smooth-wind model (blue dotted line), and a clumped model (red solid line). As anticipated, clumping hardly affects the line formation at short wavelengths. Right panel: again Mg XII, with three smooth models that assume X-ray onset radii of 1.01 R_* (blue dotted-solid line), 1.1 R_* (red solid line), and 1.5 R_* (green dashed line), suggesting that X-ray radiation *initiates* roughly at 1.1 R_* (for the adopted velocity law). The vertical lines indicate the rest wavelength shifted with the systemic velocity 15 km s^{-1}.

The right panel of Figure 15 shows a comparison between the observed Mg XII line and three smooth-wind models that assume different onset radii for the X-ray emission: 1.01 R_* (blue dotted solid line), 1.1 R_* (red solid line), and 1.5 R_* (green dashed line). This comparison clearly illustrates that X-rays must already form very close to the stellar surface, at around 1.1 R_*. Larger onset radii result in flat-topped line profiles that do not agree at all with the observed profiles. Smaller onset radii imply narrower lines than those observed. We note that the exact values are very sensitive to the adopted velocity law. However, the same conclusion is obtained for all of our test models, where we vary the exponent of the β-law in the domain $0.5 < \beta < 1.5$: X-rays are formed in the wind, and onset radii are close to the stellar surface. Note that a small onset radius does not imply that the X-ray *only* forms close to the stellar surface.

While the effect of porosity is negligible at $\lambda \lesssim 10$ Å, it should generally be taken into account when modeling lines at longer wavelengths, where the cool wind opacity increases. Figure 16 shows a comparison of the observed Fe XVII λ15.01 Å (left panel) and O VIII $\lambda\lambda$18.967, 18.972 Å (right panel) lines with models that include and neglect clumping (red solid and blue dotted lines, respectively). The wind model that neglects clumping is in poor agreement with the data, while a better agreement is reached when clumping is assumed. Nevertheless, the exact profile shape is not reproduced, especially in the case of the O VIII line. In fact, there is evidence that the widths of the

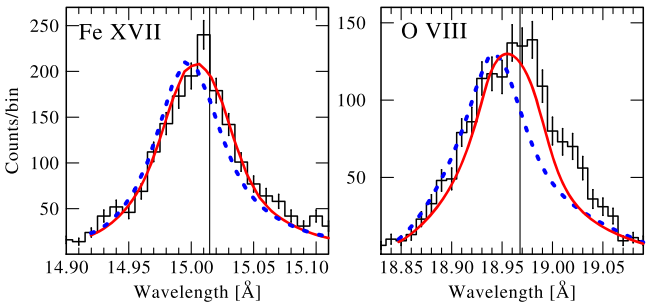

Figure 16. Left panel: observed co-added MEG±1 spectrum of δ Ori A centered on Fe XVII line (histogram) and two wind model lines: smooth (blue dotted line) and clumped (red solid line). The onset of X-ray-emitting plasma is at 1.2 R_*. Right panel: same as the left panel, but for the O VIII line.

X-ray lines in δ Ori A change with time (Paper II). Our tests indicate that the observed lines can be more accurately reproduced when fitted at each phase separately. To fit the global profiles, the variable line profiles would need to be averaged out. However, such a study, while interesting, is not the subject of this paper.

To summarize, we illustrated that clumping generally plays a role in shaping the observed X-ray lines, that the line profiles suggest small onset radii of $\sim$1.1 R_*, and that the X-ray emitting parcels are likely coupled to the cool wind.

7. SUMMARY AND CONCLUSIONS

We have performed a multi-wavelength, non-LTE spectroscopic analysis of the massive δ Ori A system, which contains the visually brightest O-type eclipsing binary in the sky and a wider tertiary component. Our goal was to obtain accurate stellar parameters for the components of the system, to analyze their winds, and to gain a better understanding of the X-ray radiation emitted from the system. Three additional studies performed within the framework of the current collaboration explore the X-ray properties (Paper I) and variability (Paper II) of the system, and conduct a complete binary and optical variabilty analysis of the system (Paper III).

We conclude the following.

1. Distance-independent parameters such as T_* and $\log g_*$ derived for the primary (see Table 1) are consistent with its spectral type O9.5 II. Distance-dependent parameters such as the luminosity and mass are found to be unusually low for the *Hipparcos* distance $d = 212$ pc. Typical values ($L_1 = 5.28\,L_\odot$, $M_1 = 24\,M_\odot$) are obtained for the distance $d = 380$ pc of the neighboring cluster. These results agree well with the results reported in Paper III, suggesting that the *Hipparcos* distance is strongly underestimated.
2. The secondary is marginally detectable in the composite spectrum. The V-band magnitude difference between the primary and secondary is constrained to $\Delta V_{\rm Aa1Aa2} \sim 2\overset{\rm m}{.}8$. The parameters of the secondary suggest that it is a B-type dwarf. The tertiary is confirmed to be a rapid rotator with $v \sin i \sim 220\,{\rm km\,s^{-1}}$, and its parameters correspond to an early B-type or a late O-type giant.
3. Rapid turbulent velocities ($\sim$200 km s^{-1}) prevail in the wind of the primary close to the stellar surface. We further find evidence for optically thick wind-inhomogeneities ("macroclumping"), affecting both strong resonance lines and X-ray lines.
4. For a clumping factor of $D = 10$, and accounting for porosity, the primary's inferred mass-loss rate is $\log \dot{M} \approx -6.4\,(M_\odot\ {\rm yr}^{-1})$. This value provides a consistent picture for δ Ori A along all spectral domains, from X-rays and UV to the optical and radio, and is furthermore in good agreement with hydrodynamical predictions.
5. Most X-rays emerging from δ Ori A are likely intrinsic to the wind of the primary. X-ray onset radii are found to be $\sim 1.1 R_*$.

While δ Ori A gives us a precious opportunity to study stellar winds and multiple systems of massive stars, there are still questions left unanswered. Does the primary really have an exceptionally low mass, luminosity, and mass-loss rate, or is the *Hipparcos* distance significantly underestimated? Did mass-transfer occur between the primary Aa1 and the secondary Aa2? Where do the clumps in the primary wind originate, and how can they be further quantified? Why do we not clearly observe X-ray emission originating in the interaction between the primary and secondary? How did the system evolve to its current state, and how will it continue to evolve? To answer these questions, efforts should be made in obtaining high S/N optical and X-ray spectra that resolve the binary Aa from the tertiary Ab and enable a proper disentanglement of the system. Moreover, further studies should provide more hints regarding the correct distance of the system. Finally, variability studies of P Cygni lines in the system should provide crucial, independent constraints on the amount of inhomogeniety in the primary's wind. Answering these questions should take us one step closer to a more complete understanding of stellar winds and of the evolution and properties of massive stars in multiple systems.

We thank the anonymous referee for constructive comments which helped to improve our paper. T.S. is grateful for financial support from the Leibniz Graduate School for Quantitative Spectroscopy in Astrophysics, a joint project of the Leibniz Institute for Astrophysics Potsdam (AIP) and the institute of Physics and Astronomy of the University of Potsdam. L.M.O. acknowledges support from DLR grant 50 OR 1302. We thank A. Valeev and S. Fabrika for kindly providing us with an optical spectrum of the system. We thank T. J. Henry and J. A. Caballero for fruitful discussions regarding system's distance. M.F.C., J.S.N., and W.L.W. are grateful for support via *Chandra* grants GO3-14015A and GO3-14015E. A.F.J.M. acknowledges financial aid from NSERC (Canada) and FRQNT (Quebec). J.M.A. acknowledges support from (a) the Spanish Government Ministerio de Economía y Competitividad (MINECO) through grants AYA2010-15 081 and AYA2010-17 631 and (b) the Consejería de Educación of the Junta de Andaluc ía through grant P08-TIC-4075. Caballero N.D.R. gratefully acknowledges his Centre du Recherche en Astrophysique du Québec (CRAQ) fellowship. Y.N. acknowledges support from the Fonds National de la Recherche Scientifique (Belgium), the Communauté Française de Belgique, the PRODEX XMM and Integral contracts, and the "Action de Recherche Concertée" (CFWB-Académie Wallonie Europe). J.L.H. acknowledges support from NASA award NNX13AF40G and NSF award AST-0807477. I.N. is

supported by the Spanish Mineco under grant AYA2012-39364-C02-01/02, and the European Union.

REFERENCES

Aerts, C., Puls, J., Godart, M., & Dupret, M.-A. 2009, A&A, 508, 409
Aldoretta, E. J., Caballero-Nieves, S. M., Gies, D. R., et al. 2015, AJ, 149, 26
Anderson, L. S. 1989, ApJ, 339, 558
Antokhin, I. I. 2011, BSRSL, 80, 549
Asplund, M., Grevesse, N., Sauval, A. J., & Scott, P. 2009, ARA&A, 47, 481
Auger, P. 1923, CRAS, 177, 169
Bagnuolo, W. G., Jr., & Bagnuolo, D. R. 1991, ApJ, 376, 266
Barbá, R. H., Gamen, R., Arias, J. I., et al. 2010, in Revista Mexicana de Astronomia y Astrofisica Conf. Ser. 38, 30
Baum, E., Hamann, W.-R., Koesterke, L., & Wessolowski, U. 1992, A&A, 266, 402
Blumenthal, G. R., Drake, G. W. F., & Tucker, W. H. 1972, ApJ, 172, 205
Bouret, J.-C., Hillier, D. J., Lanz, T., & Fullerton, A. W. 2012, A&A, 544, A67
Caballero, J. A., & Solano, E. 2008, A&A, 485, 931
Cananzi, K., Augarde, R., & Lequeux, J. 1993, A&AS, 101, 599
Cantiello, M., Langer, N., Brott, I., et al. 2009, A&A, 499, 279
Cardelli, J. A., Clayton, G. C., & Mathis, J. S. 1989, ApJ, 345, 245
Cassinelli, J. P., & Olson, G. L. 1979, ApJ, 229, 304
Castor, J. I., Abbott, D. C., & Klein, R. I. 1975, ApJ, 195, 157
Chini, R., Hoffmeister, V. H., Nasseri, A., Stahl, O., & Zinnecker, H. 2012, MNRAS, 424, 1925
Cohen, D. H., Wollman, E. E., Leutenegger, M. A., et al. 2014, MNRAS, 439, 908
Cohen, D. H., Wollman, E. E., Leutenegger, M. A., et al. 2014, MNRAS, 439, 908
Corcoran, M. F. 2003, in IAU Symp. 212, A Massive Star Odyssey: From Main Sequence to Supernova, ed. K. van der Hucht, A. Herrero & C. Esteban, 130
Corcoran, M. F., Nichols, J., Pablo, H., et al. 2015, ApJ, 809, 132
Cutri, R. M., Wright, E. L., Conrow, T., et al. 2012, yCat, 2311, 0
de Mink, S. E., Langer, N., Izzard, R. G., Sana, H., & de Koter, A. 2013, ApJ, 764, 166
Eldridge, J. J., Fraser, M., Smartt, S. J., Maund, J. R., & Crockett, R. M. 2013, MNRAS, 436, 774
ESA 1997a, The HIPPARCOS and TYCHO Catalogues (ESA-SP 1200) (Noordwijk: ESA), 12000
ESA 1997b, yCat, 1239, 10
Evans, C. J., Crowther, P. A., Fullerton, A. W., & Hillier, D. J. 2004, ApJ, 610, 1021
Eversberg, T., Lepine, S., & Moffat, A. F. J. 1998, ApJ, 494, 799
Feldmeier, A., Oskinova, L., & Hamann, W.-R. 2003, A&A, 403, 217
Feldmeier, A., Puls, J., & Pauldrach, A. W. A. 1997, A&A, 322, 878
Friend, D. B., & MacGregor, K. B. 1984, ApJ, 282, 591
Fullerton, A. W., Massa, D. L., & Prinja, R. K. 2006, ApJ, 637, 1025
Gabriel, A. H., & Jordan, C. 1969, MNRAS, 145, 241
Gies, D. R., & Lambert, D. L. 1992, ApJ, 387, 673
González, J. F., & Levato, H. 2006, A&A, 448, 283
Gräfener, G., Koesterke, L., & Hamann, W.-R. 2002, A&A, 387, 244
Gray, D. F. 1975, ApJ, 202, 148
Habets, G. M. H. J., & Heintze, J. R. W. 1981, A&AS, 46, 193
Hadrava, P. 1995, A&AS, 114, 393
Hainich, R., Rühling, U., Todt, H., et al. 2014, A&A, 565, A27
Hamann, W.-R., & Gräfener, G. 2004, A&A, 427, 697
Hamann, W.-R., Gräfener, G., & Liermann, A. 2006, A&A, 457, 1015
Hamann, W.-R., & Koesterke, L. 1998, A&A, 335, 1003
Hamann, W.-R., Koesterke, L., & Wessolowski, U. 1995, A&A, 299, 151
Harvey, A. S., Stickland, D. J., Howarth, I. D., & Zuiderwijk, E. J. 1987, Obs, 107, 205
Harvin, J. A., Gies, D. R., Bagnuolo, W. G., Jr., Penny, L. R., & Thaller, M. L. 2002, ApJ, 565, 1216
Heintz, W. D. 1980, ApJS, 44, 111
Hervé, A., Rauw, G., & Nazé, Y. 2013, A&A, 551, A83
Hillier, D. J. 1984, ApJ, 280, 744
Hillier, D. J. 1991, A&A, 247, 455
Hillier, D. J., Bouret, J.-C., Lanz, T., & Busche, J. R. 2012, MNRAS, 426, 1043
Hirschi, R. 2008, in Clumping in Hot-Star Winds, ed. W.-R. Hamann, A. Feldmeier & L. M. Oskinova (Potsdam: Univ.-Verl.), 9
Horch, E., Ninkov, Z., & Franz, O. G. 2001, AJ, 121, 1583
Howarth, I. D. 1997, Obs, 117, 335
Howarth, I. D., & Stevens, I. R. 2014, MNRAS, 445, 2878
Hummel, C. A., Rivinius, T., Nieva, M.-F., et al. 2013, A&A, 554, A52
Hurley, J. R., Tout, C. A., & Pols, O. R. 2002, MNRAS, 329, 897
Ignace, R. 2001, ApJL, 549, L119
Ignace, R., & Gayley, K. G. 2002, ApJ, 568, 954
Ignace, R., Waldron, W. L., Cassinelli, J. P., & Burke, A. E. 2012, ApJ, 750, 40
Koch, R. H., & Hrivnak, B. J. 1981, ApJ, 248, 249
Krtička, J., Feldmeier, A., Oskinova, L. M., Kubát, J., & Hamann, W.-R. 2009, A&A, 508, 841
Kudritzki, R. P., Pauldrach, A., Puls, J., & Abbott, D. C. 1989, A&A, 219, 205
Kudritzki, R.-P., & Puls, J. 2000, ARA&A, 38, 613
Lamers, H. J. G. L. M., Haser, S., de Koter, A., & Leitherer, C. 1999, ApJ, 516, 872
Lamers, H. J. G. L. M., & Leitherer, C. 1993, ApJ, 412, 771
Lamers, J. G. L. M. H., & Cassinelli, J. P. 1999, Stellar Winds (Cambridge: Cambridge Univ. Press)
Lefever, K., Puls, J., & Aerts, C. 2007, A&A, 463, 1093
Lépine, S., & Moffat, A. F. J. 1999, ApJ, 514, 909
Leutenegger, M. A., Paerels, F. B. S., Kahn, S. M., & Cohen, D. H. 2006, ApJ, 650, 1096
Lutz, T. E., & Kelker, D. H. 1973, PASP, 85, 573
Macfarlane, J. J., Cassinelli, J. P., Welsh, B. Y., et al. 1991, ApJ, 380, 564
Maeder, A. 1987, A&A, 178, 159
Maheswaran, M., & Cassinelli, J. P. 2009, MNRAS, 394, 415
Maíz Apellániz, J. 2010, A&A, 518, A1
Maíz Apellániz, J., Alfaro, E. J., & Sota, A. 2008, arXiv
Maíz Apellániz, J., Evans, C. J., Barbá, R. H., et al. 2014, A&A, 564, A63
Markova, N., & Puls, J. 2008, A&A, 478, 823
Markova, N., Puls, J., Scuderi, S., & Markov, H. 2005, A&A, 440, 1133
Martins, F., Schaerer, D., & Hillier, D. J. 2005, A&A, 436, 1049
Mason, B. D., Hartkopf, W. I., Gies, D. R., Henry, T. J., & Helsel, J. W. 2009, AJ, 137, 3358
Mayer, P., Harmanec, P., Wolf, M., Božić, H., & Šlechta, M. 2010, A&A, 520, A89
McErlean, N. D., Lennon, D. J., & Dufton, P. L. 1998, A&A, 329, 613
Meitner, L. 1922, ZPhy, 9, 131
Miller, N. A., Cassinelli, J. P., Waldron, W. L., MacFarlane, J. J., & Cohen, D. H. 2002, ApJ, 577, 951
Moffat, A. F. J. 1994, Ap&SS, 221, 467
Moffat, A. F. J., Corcoran, M. F., Stevens, I. R., et al. 2002, ApJ, 573, 191
Morel, M., & Magnenat, P. 1978, A&AS, 34, 477
Moshir, M., Kopan, G., Conrow, T., et al. 1990, in IRAS Faint Source Catalogue, version 2.0 (1990), 0
Muijres, L. E., de Koter, A., Vink, J. S., et al. 2011, A&A, 526, A32
Nazé, Y. 2009, A&A, 506, 1055
Negueruela, I., Maíz Apellániz, J., Simón-Díaz, S., et al. 2014, arXiv
Nichols, J., Huenemoerder, D. P., Corcoran, M. F., et al. 2015, ApJ, 809, 133
Oskinova, L. M. 2005, MNRAS, 361, 679
Oskinova, L. M., Feldmeier, A., & Hamann, W.-R. 2004, A&A, 422, 675
Oskinova, L. M., Hamann, W.-R., Cassinelli, J. P., Brown, J. C., & Todt, H. 2011, AN, 332, 988
Oskinova, L. M., Hamann, W.-R., & Feldmeier, A. 2007, A&A, 476, 1331
Owocki, S. P., Castor, J. I., & Rybicki, G. B. 1988, ApJ, 335, 914
Owocki, S. P., & Cohen, D. H. 2006, ApJ, 648, 565
Owocki, S. P., Gayley, K. G., & Shaviv, N. J. 2004, ApJ, 616, 525
Pablo, H., Richardson, N. D., Moffat, A. F. J., et al. 2015, ApJ, 809, 134
Palate, M., Rauw, G., Koenigsberger, G., & Moreno, E. 2013, A&A, 552, A39
Pallavicini, R., Golub, L., Rosner, R., et al. 1981, ApJ, 248, 279
Pauldrach, A. W. A., Vanbeveren, D., & Hoffmann, T. L. 2012, A&A, 538, A75
Perryman, M. A. C., & ESA (ed.) 1997, in The HIPPARCOS and TYCHO catalogues. Astrometric and Photometric Star Catalogues Derived from the ESA HIPPARCOS Space Astrometry Mission, Vol. 1200 (ESA Special Publication)
Petit, P., Louge, T., Théado, S., et al. 2014, PASP, 126, 469
Pollock, A. M. T. 2007, A&A, 463, 1111
Pols, O. R., Cote, J., Waters, L. B. F. M., & Heise, J. 1991, A&A, 241, 419
Porquet, D., Mewe, R., Dubau, J., Raassen, A. J. J., & Kaastra, J. S. 2001, A&A, 376, 1113
Prinja, R. K., & Massa, D. L. 2010, A&A, 521, L55
Puls, J. 2008, in IAU Symp. 250, Physical and Wind Properties from OB-Stars, ed. E. Bresolin, P. A. Crowther & J. Puls (Cambridge: Cambridge Univ. Press), 25
Puls, J., Kudritzki, R.-P., Herrero, A., et al. 1996, A&A, 305, 171
Raassen, A. J. J., & Pollock, A. M. T. 2013, A&A, 550, A55

Raghavan, D., McAlister, H. A., Torres, G., et al. 2009, ApJ, 690, 394
Runacres, M. C., & Owocki, S. P. 2002, A&A, 381, 1015
Sana, H., de Koter, A., de Mink, S. E., et al. 2013, A&A, 550, A107
Sander, A., Shenar, T., Hainich, R., et al. 2015, A&A, 577, A13
Schmidt-Kaler, T. 1982, in Vol. VI/2b, ed. K. Schaifers & H. H. Voigt (Berlin: Springer), 1
Seward, F. D., & Chlebowski, T. 1982, ApJ, 256, 530
Shaviv, N. J. 2000, ApJL, 532, L137
Shenar, T., Hamann, W.-R., & Todt, H. 2014, A&A, 562, A118
Simon, K. P., & Sturm, E. 1994, A&A, 281, 286
Simón-Díaz, S., Caballero, J. A., Lorenzo, J., et al. 2015, ApJ, 799, 169
Simón-Díaz, S., & Herrero, A. 2007, A&A, 468, 1063
Smartt, S. J., Dufton, P. L., & Lennon, D. J. 1997, A&A, 326, 763
Sota, A., Maíz Apellániz, J., Morrell, N. I., et al. 2014, ApJS, 211, 10
Sota, A., Maíz Apellániz, J., Walborn, N. R., et al. 2011, ApJS, 193, 24
St-Louis, N., & Moffat, A. F. J. 2008, in Clumping in Hot-Star Winds, ed. W.-R. Hamann, A. Feldmeier & L. M. Oskinova (Potsdam: Univ.-Verl.), 39
Sundqvist, J. O., & Owocki, S. P. 2013, MNRAS, 428, 1837
Sundqvist, J. O., Puls, J., Feldmeier, A., & Owocki, S. P. 2011, A&A, 528, A64
Szabados, L. 1997, in ESA Special Publication 402, Hipparcos, ed. R. M. Bonnet et al., 657
Todt, H., Kniazev, A. Y., Gvaramadze, V. V., et al. 2013, MNRAS, 430, 2302
Tokovinin, A., Mason, B. D., & Hartkopf, W. I. 2014, AJ, 147, 123
Torres, K. B. V., Lampens, P., Frémat, Y., et al. 2011, A&A, 525, A50
Unsöld, A. 1955, Physik der Sternatmosphären (Julius Springer)
Šurlan, B., Hamann, W.-R., Aret, A., et al. 2013, A&A, 559, A130
van Altena, W. F., Lee, J. T., & Hoffeit, D. 1995, yCat, 1174, 0
van Leeuwen, F. 2007, A&A, 474, 653
Villamariz, M. R., & Herrero, A. 2000, A&A, 357, 597
Vink, J. S., de Koter, A., & Lamers, H. J. G. L. M. 2000, A&A, 362, 295
Walborn, N. R. 1972, AJ, 77, 312
Waldron, W. L., & Cassinelli, J. P. 2001, ApJL, 548, L45
Waldron, W. L., & Cassinelli, J. P. 2007, ApJ, 668, 456
Waldron, W. L., & Cassinelli, J. P. 2010, ApJL, 711, L30
Weber, E. J., & Davis, L., Jr. 1967, ApJ, 148, 217
Williams, P. M., van der Hucht, K. A., Pollock, A. M. T., et al. 1990, MNRAS, 243, 662
Zahn, J.-P. 1975, A&A, 41, 329